Critical phenomena in helical rods with perversion

Émilien Dilly, Sébastien Neukirch, J. Derr, Dražen Zanchi

Critical phenomena in helical rods with perversion

Émilien Dilly[a,b], Sébastien Neukirch[c], Julien Derr[b], Dražen Zanchi[a,*]

[a] *Laboratoire Matière et Systèmes Complexes, UMR 7057, Université Paris Cité, CNRS, F-75205 Paris Cedex 13, France*

[b] *Laboratoire Reproduction et Développement des Plantes, École Normale Supérieure de Lyon, CNRS, INRAE, Inria, 69364 Lyon Cedex 07, France*

[c] *Institut Jean Le Rond d'Alembert, CNRS (UMR 7190), Sorbonne Université, 75005 Paris, France*

Abstract

Equilibrium configurations of helical elastic rods during quasi-static unwinding are studied experimentally and theoretically. At a critical degree of unwinding, the helical conformation destabilizes into a mixed phase consisting of two helices with opposite chiralities connected by a perversion. As unwinding progresses, the perversion migrates along the rod, eventually disappearing, leading to a pure helical conformation with opposite chirality from the initial state. Measurements of axial torque and force as functions of extension and winding reveal remarkable phenomena: (i) As the perversion migrates, the torque remains nearly constant. (ii) The transition from a pure helix to a configuration with perversion is accompanied by snapping events, seen as singularities in torque and force. (iii) At a critical force, the perversion destabilizes and transitions to a self-touching conformation. The phase diagram and overall mechanical behavior are reproduced using a biphasic model. A shooting technique, numerical path-following methods and finite element simulations are employed to assess the instability of the perversion and the associated snapping toward self-contact. The singularity at the creation of the perversion is reproduced by incorporating clamping effects within path-following methods. An analogy with first-order phase transitions is discussed. The nearly constant torque in the mixed phase is reminiscent of a Maxwell plateau, while the creation of a perversion with snapping corresponds to a nucleation event. Finally, to apply our analysis to plant tendrils, we study a specific line in the phase diagram of the mixed state corresponding to zero net turns. The associated transition is continuous and supercritical.

1. Introduction

Helices are ubiquitous in nature and because of their geometrical simplicity they have always attracted much attention (Cook, 1979; Chouaieb et al., 2006; Forterre and Dumais, 2011). The equations for the behavior of helical elastic rods have been established long ago (Kirchhoff, 1859; Love, 1990; Timoshenko and Gere, 1961), but there is a resurgent interest in twisted elastic rods over recent decades with applications across various scientific domains such

*Corresponding author
Email address: drazen.zanchi@u-paris.fr (Dražen Zanchi)

as single-molecule DNA nanomechanics (Strick et al., 1996; Allemand et al., 1998; Bryant et al., 2003; Sarkar et al., 2001; Bustamante and Yan, 2022; Marko and Neukirch, 2013) or soft robotics and microengineering (Jones et al., 2021; Mehling et al., 2006; Lutz-Bueno et al., 2020; Armanini et al., 2023; Jones et al., 2021), propelling flagella of microorganisms (Goldstein et al., 2000; Nakane et al., 2020; McGuffee et al., 2023) and even electrospun microfibrils (Canejo and Godinho, 2013; Silva et al., 2016). Theoretical efforts to decipher possibilities of destabilization of a purely helical conformations have been reported (Zhou et al., 2007; Borum and Bretl, 2020). The renewed efforts in the exploration of soft filamentous structures for executing mechanical actions prompts inquiries into their mechanical behavior and the quest for novel functionalities. In this context, in the present paper we focus specifically on the perversions in helical rods and in particular on deciphering possible critical conformation changes involving perversion.

Perversion is a topological formation connecting two domains of opposite chiralities. The term is attributed to Listing (1848) and was popularized by Maxwell (1873, page 25), see also Goriely and Tabor (2013). In the context of elastic rods, perversions manifest as an intriguing phenomena, unveiling captivating physics at our fingertips. When unwinding an elastic helix by decreasing the number of coils, a critical point is reached where a helix with opposite chirality emerges (Dilly et al., 2023). The connection between the two helices is a perversion. As the unwinding continues, the perversion migrates, causing the helix of opposite chirality to grow while the original one shrinks. Eventually, the perversion reaches the opposite side and is absorbed by the clamp, resulting in a pure helix of opposite chirality. Further rotation in the same direction leads to the overwinding of this helix. This seemingly straightforward experiment highlights multiple non-trivial mechanical effects. The rich physics of perversions in elastic systems already motivated considerable theoretical work. Dai et al. (2018) evidenced the non trivial behaviour of overwinding then unwinding as a function of extension. Based on finite element simulations, Wang et al. (2020) showed the very localized character of perversions, and the possibility to treat them as point defects. Other authors discussed the possibility of equilibrium with multiple perversions (Domokos and Healey, 2005; Riccobelli et al., 2021).

The generation of perversion also arises in many biological systems, ranging from the small scale with propelling flagella of microorganisms (Goldstein et al., 2000; Nakane et al., 2020) and fibers in spider webs (Canejo and Godinho, 2013) to the macroscopic scale with tendrils of climbing plants (Darwin, 1865; Gerbode et al., 2012). Darwin, intrigued by the coiling behavior of tendrils, remarked, "when a tendril has caught a support and is spirally contracted, there are always as many turns in one direction as in the other; so that the twisting of the axis in one direction is exactly compensated by the twisting in the opposite direction" (Darwin, 1865). An easy way to reproduce the appearance of perversion, resembling that of what happens in plants, is by taking an elastic helix, straightening it, and rotating it so that the total number of turns in the rod becomes zero ($n = 0$). By decreasing the axial force applied to the rod or, equivalently, approaching the two extremities, two helices of opposite chirality appear, connected again by a perversion. This so-called writhing instability has been theoretically studied and was given as an explanation for tendril writhing (Goriely and Tabor, 1998; McMillen and Goriely, 2002). Past studies on the mechanics of perversions and the writhing instability mainly focused on either inhomogeneous pre-stressed rods (Liu et al., 2014, 2016) or intrinsically curved yet untwisted filaments (McMillen and Goriely, 2002).

In the present paper we report experimental and theoretical study of helical rods subjected to rotation n and extension z for intrinsically uniformly curved and twisted axially clamped rods. We focus particularly on identifying and rationalizing different critical phenomena in the system with perversion. After assessing the stability diagram, see fig. 5, we focus on the ways in which the perversion is induced or destabilized. Namely, the injection/annihilation of the perversion (red line crossing in fig. 5) and the perversion collapse into a self-contact (blue line crossing in fig. 5) are singular snapping events. One of core issues of the present paper is the theoretical description of these singular events. Finally, in order to approach the case of plant tendrils where the rod is unwound ($n = 0$), we study in detail the writhing transition which is yet another critical phenomenon, see fig. 13.

The manuscript is organized as follows. In section 2, we report experimental results of helices unwinding. We

detail the experimental setup, describe the unwinding process of a helix, and assess a phase diagram for the stability of different configurations as a function of number of turns and extension. Section 3 brings a quantitative theoretical understanding of our experimental measurements. We use the Kirchhoff theory ofx elastic rods to discuss the properties of connected helices and predict the phase diagram of helical configurations by assuming a biphasic model which neglects the perversion. We then use shooting methods to find the perversion solution and discuss the conditions under which this solution exists or disappears as the helices jump to self-contact. Finally, we discuss finite-size effects revealed by full numerical solutions. The injection and expulsion of perversion are thereby identified as sub-critical bifurcations. Section 4 is dedicated to the analysis of a particular line of the phase diagram, when the number of turns remains null ($n = 0$). This is the writhing transition which we investigate both experimentally and theoretically. In section 5, we discuss our results and develop the analogy with phase transitions. In particular, the perversion injection events are discussed in comparison with heterogeneous nucleation in first-order phase transitions. We also discuss the Maxwell-like plateau in the transition and we anticipate the characteristics of a system with more than one perversion. The section 6 contains concluding remarks.

2. Experiments

2.1. Materials and methods

Elastic helices were elaborated from the two-component elastomer paste AWASIL Novo 90 Silikon-Knetmasse from Wagner Dental®. The mixed paste was extruded from a circular syringe nozzle and then manually wrapped around a metallic cylinder on which the helical pattern had been drawn. The obtained material's Young modulus was estimated to be $Y = 5 \pm 2$ MPa through the measurement of the oscillating frequency of a straight rod segment. The Poisson ratio of the material was estimated to be $\nu = 0.5$, as usual for such materials. This helix is made right-handed (it turns clockwise) and we will denote its chirality by (+), while the opposite chirality is called (-).

The obtained helical rod is placed in the experimental setup presented in fig. 1(a). It is fixed in two mandrels such that the tangent vector to the rod is vertical at the clamping points of the rod. The two mandrels are then aligned vertically through the use of horizontal manual micro-translation stages. The upper mandrel is fixed on a motorized rotation stage 8MR174(E)-11-28 from Standa®, having a resolution of 0.015°. The lower mandrel was axially fixed to a reaction torque sensor TFF400-FSH03982 from Futek® having a resolution of 10^{-4} mN·m. The torque-meter is placed on a Kern® KB 360-3N scale to allow for vertical axial force measurements. The scale had precision 0.001 g. The whole lower apparatus was placed on a vertical translation Standa® 8MT175 motorized stage with a resolution of 2.5 μm, to allow for vertical displacement of the lower end of the rod.

2.2. Helix unwinding experiments

A helix with radius $R_0 = 3.9$ mm, pitch $P_0 \equiv z_0/n_0 = 4.7$ mm, cross-section diameter $d = 1.7$ mm, number of coils in its unloaded state $n_0 = 9.5$, and total arc length $L = 0.24$ m is manufactured and clamped in the experimental setup as described above (see fig. 1(b) for notations). It is clamped in its resting configuration so that its number of coils and its extension approximately correspond to (n_0, z_0). The extension is then changed to the value z using the translation stage. Next, using the rotation stage, the helix is progressively unwound as shown in fig. 2(a). At a critical number of turns, the helix destabilizes in a discontinuous transition, nucleating a perversion at one end of the rod. With further rotation, the perversion migrates along the rod, increasing the portion of the $(-)$ helix Ultimately, the perversion disappears at the opposite end from where it was nucleated, leaving a pure $(-)$ helix.

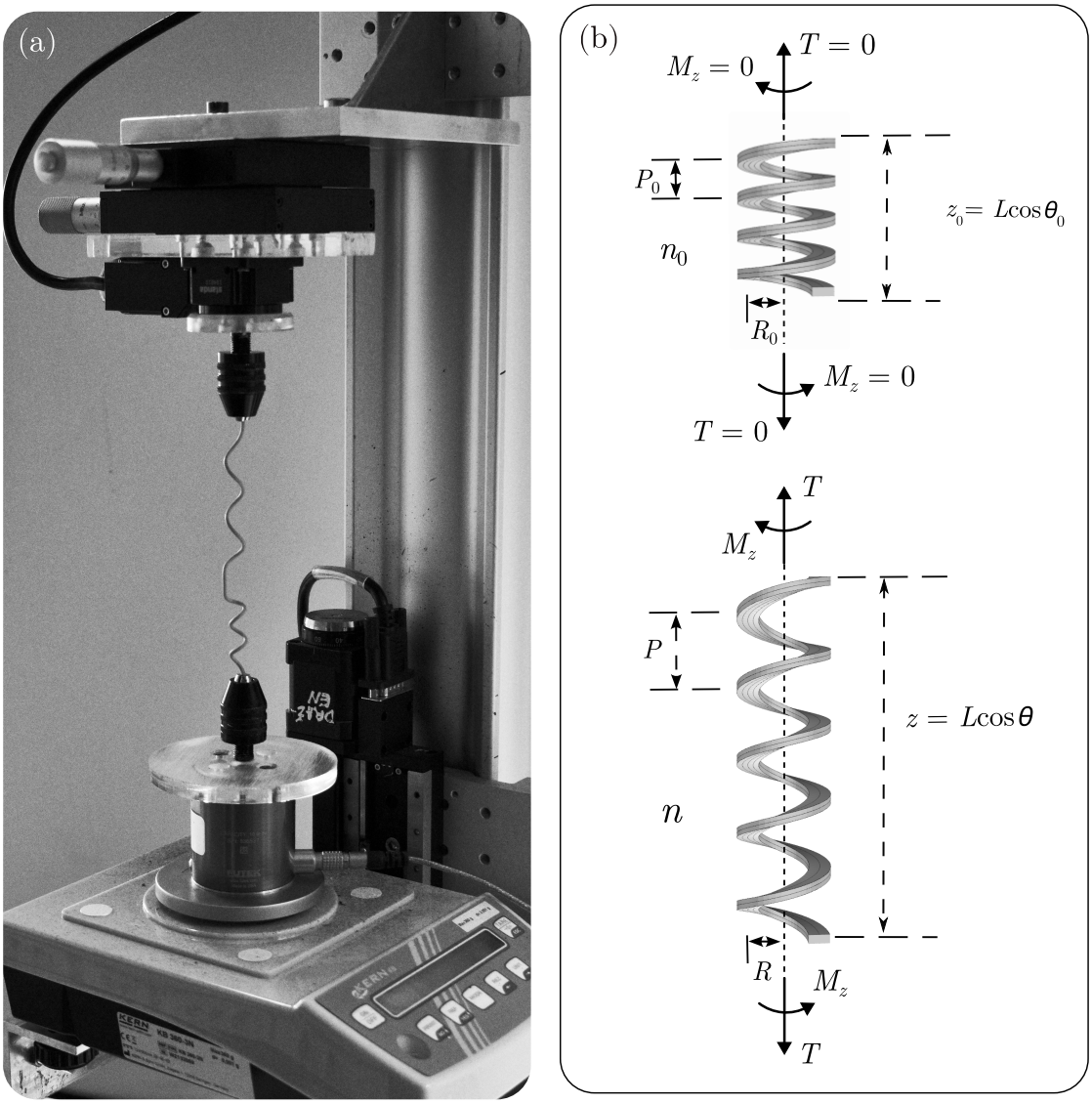

Figure 1: (a) Experimental setup. A helical rod made of elastomer is held between two vertically aligned mandrels. The upper mandrel is fixed to a rotation stage, while the lower mandrel is mounted on a torque-meter, which rests on a scale for vertical force measurements. The scale is positioned on a translation stage to control the rod extension. (b) Schematic representation of a helix in its intrinsic state under no external constraints and in its actual, loaded state. A helix has intrinsic extension z_0 and intrinsic number of coils n_0 under no external constraints. Under axial force T and torque M, the helix has a number of coils n and extension z. The pitch and radius of the helix are P_0 and R_0 in the unloaded state and P and R in the loaded state.

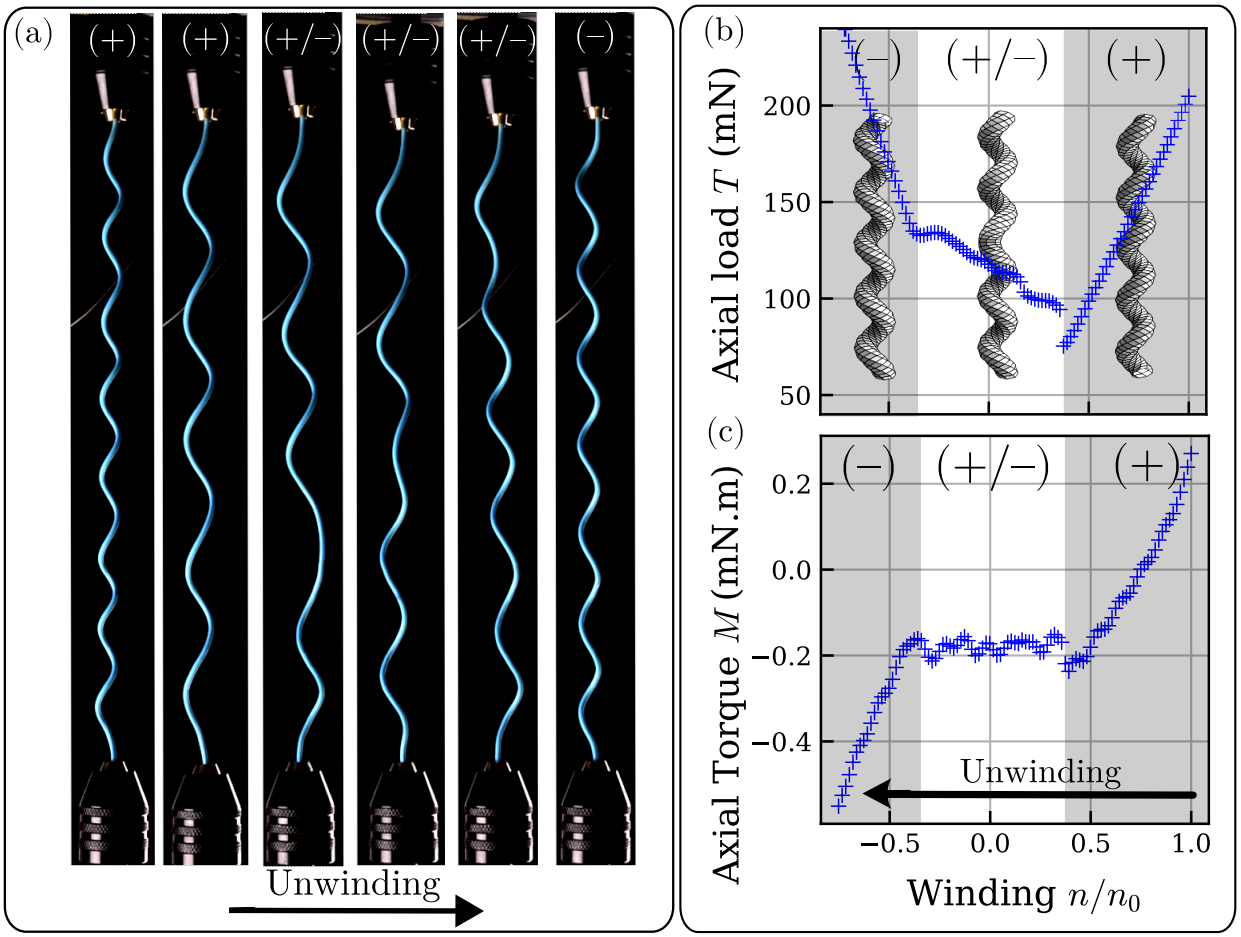

Figure 2: (a) Snapshots during the unwinding experiment of helical rod with initially (+) chirality at $z/L = 0.86 \pm 0.02$. By counter rotation of the upper mandrel, the number of coils in the helix decreases. At a critical number of turns, a perversion is nucleated and two helices of opposite chiralities are connected in configuration (+/−). Finally, at another critical number of turns, perversion disappears at the opposite extremity leaving the pure helix (−) helix. (b) Axial force and (c) axial torque during the unwinding of a rod with $z_0/L = 0.2$ at extension $z/L = 0.91 \pm 0.02$.

Throughout the unwinding process, the axial torque M and force T are measured, see fig. 2(b). The different events described above can be correlated with specific changes in the axial torque and force. As the helix of pure (+) chirality is unwound, the axial torque and force decrease. Upon the formation of the perversion, a jump in axial torque and force is observed. During the presence of the perversion, the monotonic behavior of the axial force is reversed: it now increases as unwinding continues. In contrast, the axial torque remains nearly constant compared to the pure helix case, exhibiting oscillations as the perversion migrates. Once the perversion has fully migrated along the rod and has disappeared at the mandrel, yielding the pure (−) helix, the axial force increases with a steeper slope and the axial torque resumes decreasing, with a slope comparable to that of the (+) helix regime. A jump in both M and T is obvious on injection of perversion upon unwinding. On the other side of the coexistence region, upon unwinding, only a weaker transition is observed. The above observations are indications that helix inversion is a subcritical phenomenon.

The critical values of n at which the perversion is nucleated and disappears, and therefore the range of n at which the coexistence between (−) and (+) helices is observed, depend on the extension z of the rod. This is the subject of the next section.

2.3. Phase diagram assessment

The following experiment is aimed at constructing the stability diagram of the rod in the (n, z) plane. We start at an extension $z/L = 0.5$ and with a number of turns n such that there is a coexistence between a (−) helix and a (+) helix, connected by a perversion. The rod in this mixed state (+/−) is then stretched, as depicted in fig. 3(a). At a critical extension z, in a similar manner to the previous section, the perversion disappears, yielding a pure helix of either (+) or (−) chirality. The corresponding experimental axial torque and force profiles from this experiment are displayed in fig. 3(b) for several values of the winding ratio $n/n_0 = 0.58 \pm 0.04; 0.75 \pm 0.04; 0.83 \pm 0.04$. We see that the axial force increases with the extension both before and after the disappearance of the perversion. In the axial torque profiles, we note two distinct regimes, with a slope discontinuity (most visible on the light blue curve) occurring concomitantly with the disappearance of the perversion.

This experiment was repeated for a range of winding ratios n/n_0 between -1 and 1. The corresponding axial torque and force profiles as functions of both the extension z and the number of turns n are displayed in fig. 4(a) and (b). The slope discontinuity corresponding to the appearance/disappearance of the perversion is clearly visible. It agrees fairly well with the domain limit (red line) of existence of the mixed state obtained within the biphasic model, as will be presented in section 3.2.

We are now ready to construct the phase diagram. The values of $z(n)$ at which the slope discontinuity occurs are shown as black crosses in fig. 5. Below the black crosses, the mixed state (+/−) is stable, while above it the rod is a pure helical state. We see that the larger the extension, the narrower the mixed-state region is.

3. Theory

In this section, we present a framework for the quantitative understanding of the experimental results presented in Section 2. The standard theory for calculating equilibriums of elastic curved rods is the Kirchhoff theory (Kirchhoff, 1859; Love, 1990; Antman, 2004; Audoly and Pomeau, 2010). We first present the general formulation of the biphasic model, neglecting the presence of the perversion and the presence of the clamping boundary conditions. Second, we

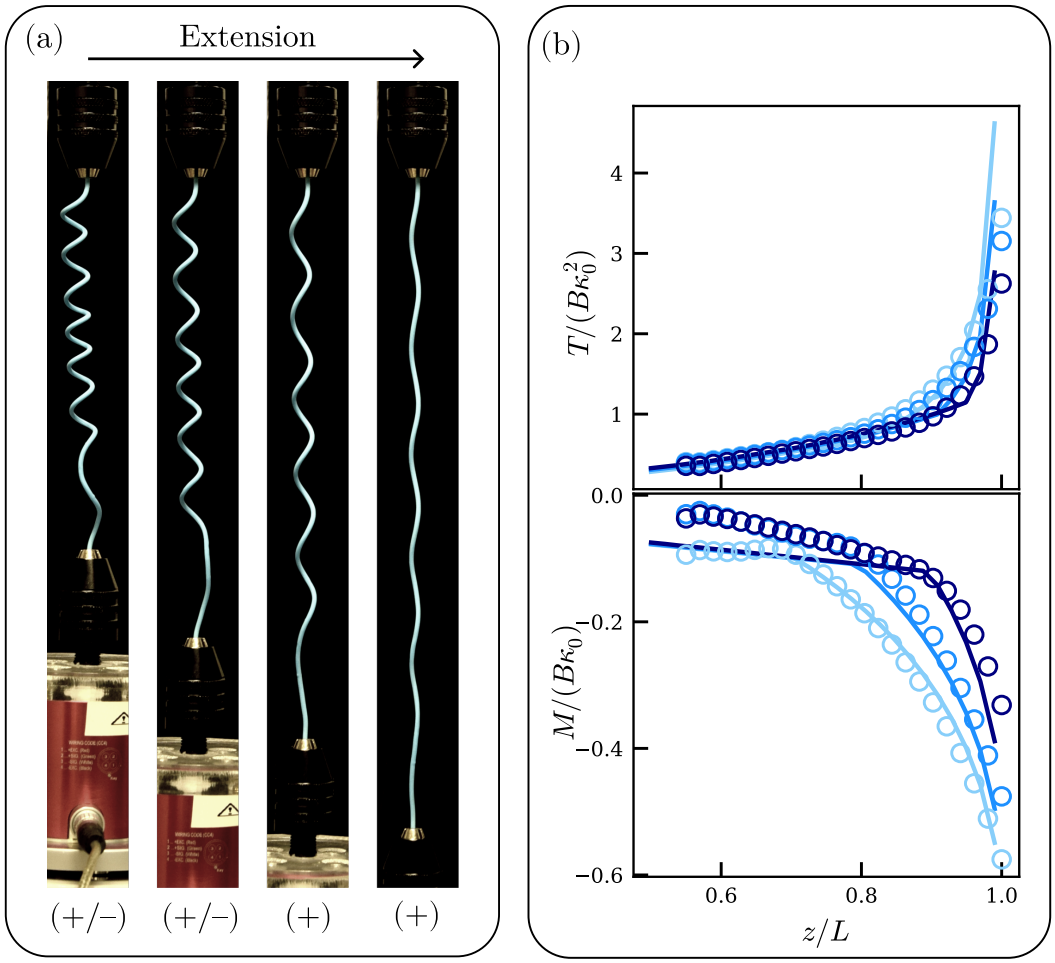

Figure 3: (a) Extension experiments of the $(+/-)$ configuration. By unwinding the helix, the rod is first prepared in $(+/-)$ state, and then extended. At a critical value of extension the perversion disappears, yielding either a purely positive or a purely negative helix depending on the imposed number of turns. (b) Dots - Axial force T and torque M for extension experiments for several winding ratios: light blue, $n/n_0 = -0.58 \pm 0.04$; blue -0.75 ± 0.04 ; dark blue, -0.83 ± 0.04 ; helix with $z_0/L = 0.2$. Lines of the corresponding colors are calculated within the biphasic model with $\Gamma = 2/3$.

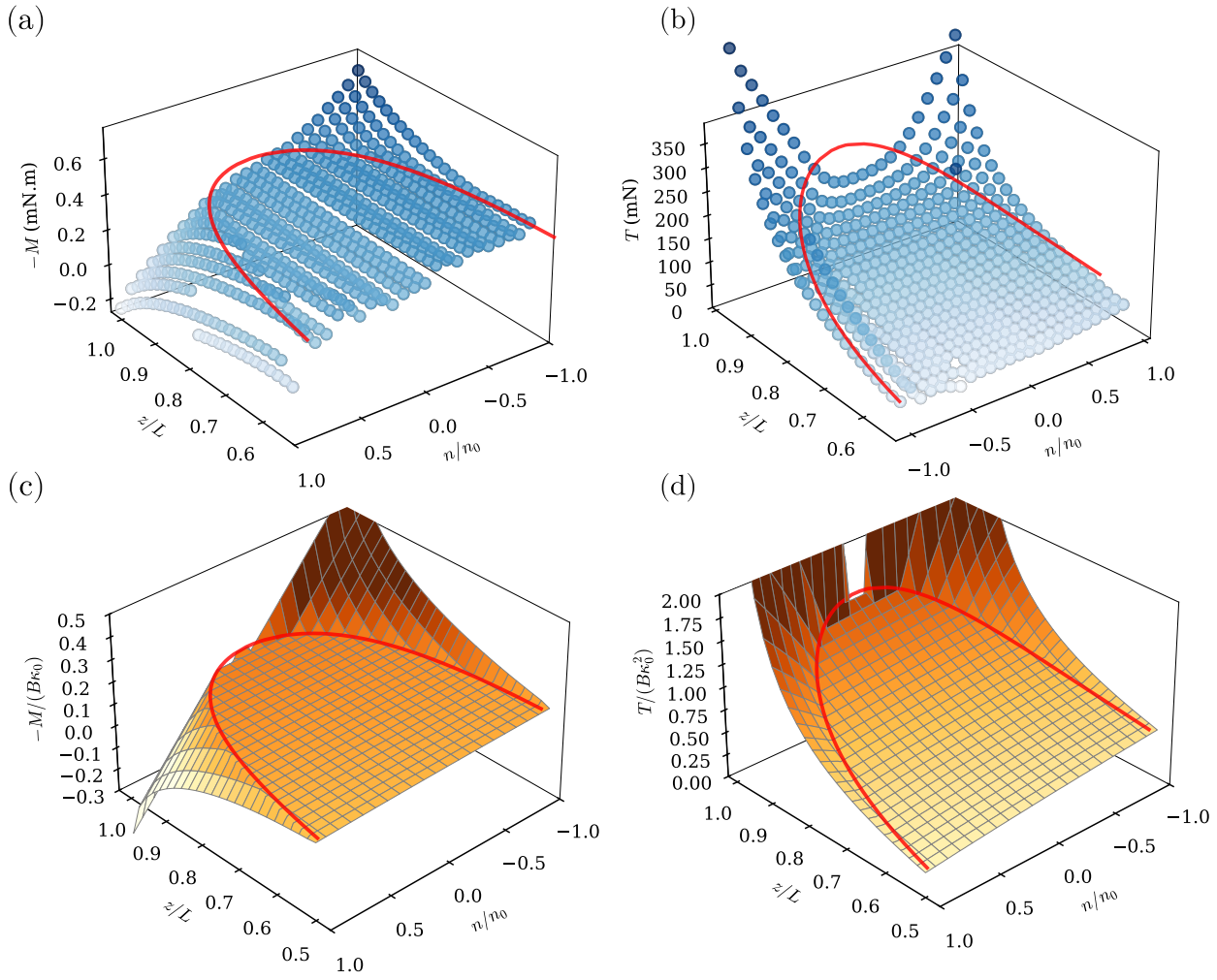

Figure 4: In blue are axial torque M (a) and force T (b) obtained by extension experiments of $(+/-)$ configuration -see fig. 3(a)- for a range of n/n_0 in $[-1:1]$, helix with $z_0/L = 0.2$. Panels (c) and (d): calculated axial torque M and force T biphasic model. The red lines depict M (panels (a) and (c)) and T (panels (b) and (d)) at the limit of existence of $(+/-)$ state in the biphasic model. Fixed parameters are $z_0/L = 0.2$ and $\Gamma = 2/3$.

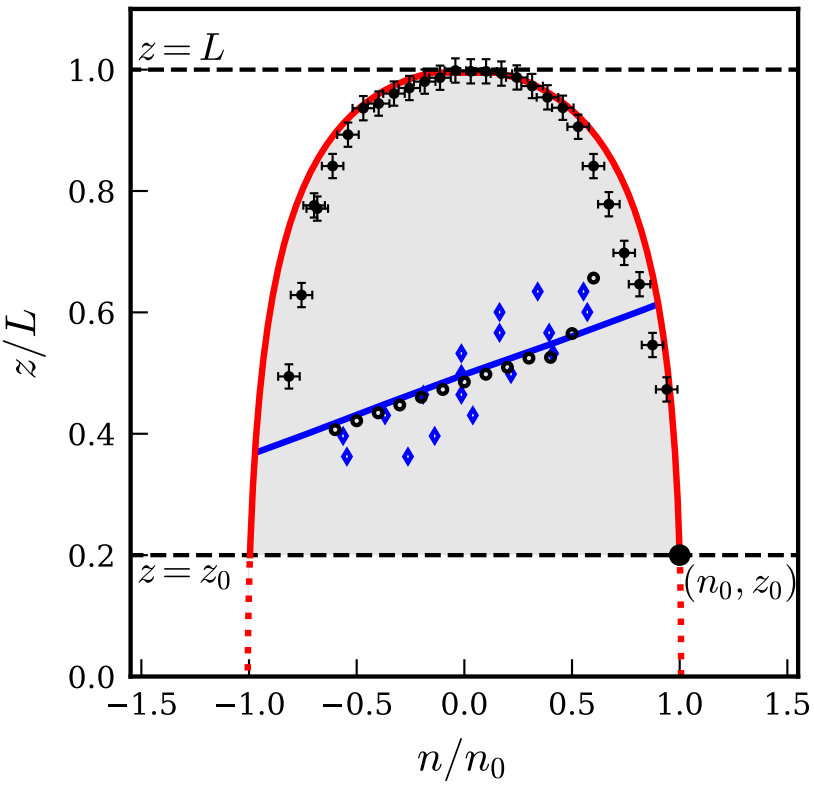

Figure 5: Stability diagram of helical rod in (n, z) plane. Black crosses: extension at which the measured axial torque presents a slope discontinuity as shown in fig.2(b), corresponding to disappearance of perversion (data taken from (Dilly et al., 2023), helix with $z_0/L = 0.2$ and $\Gamma = 2/3$). Red curve: limit of existence of $(+/-)$ phase obtained with the biphasic model. Blue line: critical tension at which the perversion solution vanishes within the shooting method. Blue diamonds: transition from self-contact to non-self-touching perversion in the unwinding experiments. Black circles: extension at which the $(+/-)$ conformation with non-self-touching perversion destabilizes in AUTO simulations. In all calculations $\Gamma = 2/3$ and $z_0/L = 0.2$.

use a shooting method to compute the perversion solution while still neglecting the clamps. The shooting method is also validated against 3D finite element simulations. Third, we solve nonlinear boundary value problem using the AUTO package to consider both clamping and perversion effects.

3.1. Kirchhoff theory and connection of helices

The Kirchhoff theory of elastic rods considers unshearable and inextensible rods with bending and twisting deformations related linearly to corresponding stresses (Audoly and Pomeau, 2010). The rod is described by its centerline curve $\mathbf{r}(s)$, parametrized by the arc length s. The tangent vector $\mathbf{d_3}(s)$ is defined by

$$\mathbf{r}'(s) = \mathbf{d_3}(s) \tag{1}$$

Two other vectors $(\mathbf{d_1}(s), \mathbf{d_2}(s))$ are attached to the cross-section of the rod and the frame $(\mathbf{d_1}(s), \mathbf{d_2}(s), \mathbf{d_3}(s))$ is taken orthonormal and called director basis or material frame. This orthonormality implies the existence of a curvature vector $\boldsymbol{\kappa} = (\kappa_1(s), \kappa_2(s), \kappa_3(s))$ that keeps track of the orientation change of the director basis along the center-line

$$\mathbf{d_i}'(s) = \boldsymbol{\kappa} \times \mathbf{d_i}(s) \tag{2}$$

At equilibrium, due to force and moment balance on the cross-section of the rod, the internal force $\mathbf{T}(s)$ and internal moment $\mathbf{M}(s)$ satisfy the static Kirchhoff equations:

$$\mathbf{T}'(s) = 0 \tag{3a}$$

$$\mathbf{M}'(s) + \mathbf{d_3}(s) \times \mathbf{T}(s) = 0. \tag{3b}$$

Finally, the constitutive relations link the internal torque $\mathbf{M}$ with the deformation field $\boldsymbol{\kappa}$ through the relations

$$\mathbf{M}(s) \cdot \mathbf{d_i}(s) = B_i \ [\kappa_i(s) - \kappa_{i0}(s)] \tag{4}$$

where the $\kappa_{i0}(s)$ describe the natural shape of the rod, i.e. the shape of the rod when it is free of forces and torques. In this unstressed state, the rod would have uniform curvatures κ_{i0} and its shape would be perfectly helical. The coefficients B_i correspond to bending rigidities in the $\mathbf{d_1}$ and $\mathbf{d_2}$ directions and are equal in the case of a rod with axisymmetric cross-section, $B_1 = B_2 = B$. Finally, $B_3 = C$ corresponds to the twist rigidity of the rod. We suppose, without loss of generality, that the considered rod has intrinsic curvature κ_0 in the $\mathbf{d_1}$ direction, zero intrinsic curvature in the $\mathbf{d_2}$, and intrinsic torsion τ_0 in the $\mathbf{d_3}$ direction. In the experimental case presented in section 2, where the rod material is uniform and isotropic, and the section of the rod is circular, we have $B_1 = B_2 = B = YI$ and $B_3 = C = YI/(1+\nu)$, Y being the Young modulus, $I = \pi d^4/64$ is the second moment of the circular cross section and ν the Poisson ratio. The intrinsic curvature and torsion κ_0 and τ_0 can be linked to the intrinsic radius R_0 and pitch P_0 (see fig.1) through the formulas

$$\begin{aligned} \kappa_0 &= R_0 \left(R_0^2 + \frac{P_0^2}{4\pi^2} \right)^{-1} \\ \tau_0 &= \frac{P_0}{2\pi} \left(R_0^2 + \frac{P_0^2}{4\pi^2} \right)^{-1} \end{aligned} \tag{5}$$

These formulas also hold if we express the actual state κ, τ as a function of the actual radius R and pitch P. If we project system (3) in the director basis, we obtain

$$\begin{aligned} T_1' &= T_2\kappa_3 - T_3\kappa_2 \\ T_2' &= T_3\kappa_1 - T_1\kappa_3 \\ T_3' &= T_1\kappa_2 - T_2\kappa_1 \\ \kappa_1' &= T_2/B + (1-\Gamma)\kappa_3\kappa_2 + \Gamma\tau_0\kappa_2 \\ \kappa_2' &= -\left[T_1/B + (1-\Gamma)\kappa_3\kappa_1 - \kappa_0\kappa_3 + \Gamma\tau_0\kappa_1\right] \\ \kappa_3' &= -\frac{\kappa_0\kappa_2}{\Gamma} \end{aligned} \tag{6}$$

where we have introduced $\Gamma = C/B = 1/(1+\nu)$. Eq. (6) can be interpreted as a six-dimensional dynamical system for $\mathbf{T}(\mathbf{s})$ and $\boldsymbol{\kappa}$, where the arc-length s is the analog of time. It can be shown from Eq. (3) that the quantities

$$I_1 = \kappa_1^2 + \kappa_2^2 + \Gamma\kappa_3^2 + 2T_3/B_1 \tag{7a}$$

$$I_2 = \mathbf{T}^2 \tag{7b}$$

$$I_3 = B(\kappa_1 - \kappa_0)T_1 + B\kappa_2 T_2 + \Gamma\kappa_3 T_3 \tag{7c}$$

are conserved along the rod (McMillen and Goriely, 2002). It can also be shown that helices of curvature vector $\boldsymbol{\kappa}_h = (\kappa, 0, \tau)$ and force vector $\mathbf{T} = (\gamma\tau\kappa, 0, \gamma\tau^2)$, with $\gamma = \kappa_0/\kappa - 1 + \Gamma(1-\tau_0/\tau)$, are solutions of system (6). Throughout this paper, and similarly to (McMillen and Goriely, 2002), we use the convention that helices with negative torsion have negative chirality. The force and torque vectors are aligned with the helix axis, and if we call z the helix axis we have $\mathbf{T} = T\mathbf{e_z}$, and $\mathbf{M}\cdot\mathbf{e_z} = M$, with

$$T = B\gamma\chi\tau\sqrt{\kappa^2+\tau^2} \tag{8a}$$

$$M = B\chi(\kappa^2+\tau^2)^{-1/2}\left[\kappa(\kappa-\kappa_0) + \Gamma\tau(\tau-\tau_0)\right]. \tag{8b}$$

where we note $\chi = \pm 1$ the chirality of the helix in the actual conformation.

We now consider two Kirchhoff helices, respectively of curvature and torsion (κ_+, τ_+) and (κ_-, τ_-), that are both solutions of eq. (6) and we connect them to form a compound system. We express the three quantities introduced in eq. (7) as functions of the curvature and torsion of each helix. As these quantities are conserved along the compound system, this yields three relations between the curvatures (κ_+, κ_-) and torsion (τ_+, τ_-)

$$I_1 = \kappa_+^2 + (\Gamma + 2\gamma_+)\tau_+^2 = \kappa_-^2 + (\Gamma + 2\gamma_-)\tau_-^2\,, \tag{9a}$$

$$\frac{T}{B} = \gamma_+\tau_+\sqrt{\kappa_+^2+\tau_+^2} = -\gamma_-\tau_-\sqrt{\kappa_-^2+\tau_-^2}\,, \tag{9b}$$

$$\frac{M}{B} = (\kappa_+^2+\tau_+^2)^{-1/2}\left[\kappa_+(\kappa_+-\kappa_0) + \Gamma\tau_+(\tau_+-\tau_0)\right] = -(\kappa_-^2+\tau_-^2)^{-1/2}\left[\kappa_-(\kappa_--\kappa_0) + \Gamma\tau_-(\tau_--\tau_0)\right] \tag{9c}$$

with $\gamma_\pm = \kappa_0/\kappa_\pm - 1 + \Gamma(1-\tau_0/\tau_\pm)$. The second and the third equations can be seen as force and torque conservation between the two helices. There are four variables $(\kappa_+, \tau_+, \kappa_-, \tau_-)$ and three equations in (9). Accordingly, the set of connected helices must lie on one or several 1D curves in the (κ, τ) space. In the special case $\tau_0 = 0$, where the rod has a circular shape in its intrinsic state, equations (9) reduces to $\kappa_+ = \kappa_-, \tau_+ = \tau_-$ and $(\kappa-\kappa_0)\kappa + \Gamma\tau^2 = 0$, which corresponds to an ellipse in the (κ, τ) space, as found by McMillen and Goriely (2002). In the case of $\tau_0 > 0$, equations (9) were numerically solved for $z_0 = 0.3$ and the results are shown in fig. 6(b). The red curve depicts the set of connectable helices in κ, τ space, normalized by the intrinsic curvature κ_0 of the rod. For every point - helix - on this curve, there exists a unique other point - helix - to which it can be connected. We materialize these connections with the black lines. We remark that, in most cases, a helix on the red curve is connected to a helix of opposite torsion, therefore meaning that a helix of positive chirality is in most cases connected to a helix of negative chirality. Exceptions lie near the intrinsic state (blue point) and near the straight rod (where both curvature and torsion are zero). In these cases, the connected helices have the same chirality, positive near the intrinsic state and negative near the straight rod.

Now that we know the set of possible connected helices, we have to check which couple of helices are allowed in the presence of prescribed number of turns and extension. This is done using a biphasic representation of the connected helices.

3.2. Neglecting perversion and boundaries: biphasic model

The existence of a pseudo-plateau in the $M(n)$ profile within the mixed state (+/-), as sown in fig. 2(b), motivates the development of a biphasic model. We aim to reproduce the domain boundary of the mixed state (+/−) and the

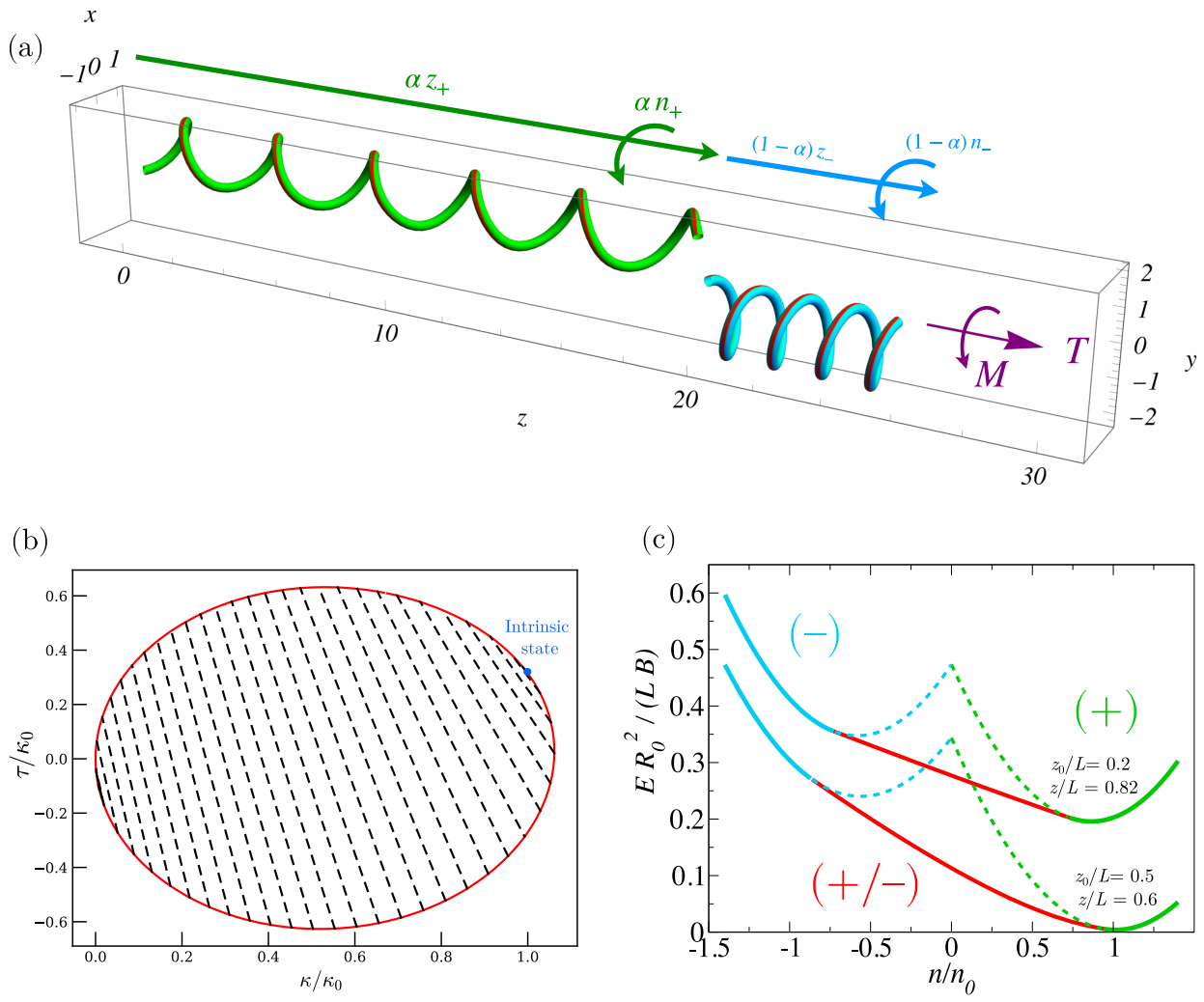

Figure 6: (a) Schematic view of the mixed state (+/−) in biphasic model: (+) segment is in green and (−) segment is in blue. (b) Red curve: profile of all connectable helices configurations for $z_0/L = 0.3$. Dashed lines: correspondences between two connected helices in (+/−) state. Each point on the red curve is connected to another unique point. (c) Calculated elastic energy of three states (+), (+/−) and (−) in black, green and red respectively, for two choices of z_0 and z. Notice that the red line is not straight. Dashed lines correspond to unstable states due to their higher energy compared to the mixed state (+/−). Fixed parameter in (b) and (c): $\Gamma = 2/3$.

corresponding mechanical signatures in terms of both axial torque M and force T. A movie illustrating the biphasic model can be seen in Supplemental Material (Dilly et al., 2024, video 1).

To search for a mixed-state solutions connecting two helices of opposite chiralities satisfying extension z and number of turns n, we suppose that the solution is a juxtaposition of two helical segments (+) and (−) (see fig.6(a)) of respective curvature and torsion (κ_+, τ_+) and (κ_-, τ_-). We suppose that the (+) helix is present in proportion α in terms of arclength, and that the (−) helix is present in proportion $(1-\alpha)$. In doing so, we neglect the effects of perversion and boundaries. Namely, the perversion and boundary layer near the clamps are not helical solutions and correspond to particular trajectories in (κ, τ) space, while helices are the uniform solution to eq. (6). In the case of an infinitely long rod, $n_0 \to \infty$, the effects of the perversion and the boundary layer in the total extension z and number of turns n of the rod become negligible and we express z and n as functions of numbers of turns and extensions of the two connected helices (see fig. 6(a)).

$$n = n_+ + n_- \tag{10a}$$

$$z = z_+ + z_-. \tag{10b}$$

Expressing the number of turns and the extension in both helices in terms of curvature and torsion yields

$$z = \alpha L \frac{\chi_+ \tau_+}{\sqrt{\kappa_+^2 + \tau_+^2}} + (1-\alpha) L \frac{\chi_- \tau_-}{\sqrt{\kappa_-^2 + \tau_-^2}} \tag{11a}$$

$$n = \alpha \chi_+ \frac{L}{2\pi} \sqrt{\kappa_+^2 + \tau_+^2} + (1-\alpha) \chi_- \frac{L}{2\pi} \sqrt{\kappa_-^2 + \tau_-^2}, \tag{11b}$$

where $\chi_\pm$ stands for the chirality of the connected helices. As mentioned above, in most cases $\chi_- = -1$, and $\chi_+ = 1$. System (11), together with eq. (9), yields a system of five equations. At given n and z, this system has five unknown, namely $(\kappa_+, \tau_+, \kappa_-, \tau_-, \alpha)$, it can be solved numerically, yielding a given couple of helices on the red curve of fig. 6(b), together with their proportion in terms of arclength α. This proportion must remain between 0 and 1, and if it is the case, there is a couple of connected helices satisfying the conditions on extension and number of turns at a given α. This domain of existence is represented in fig. 5 as the gray shaded area. The limit of this domain of existence of the connected helices is represented by the red line in fig. 5, corresponding either to the curve where $\alpha = 1^-$ or 0^+. For extension and number of turns in the white area, no solution with α comprised between 0 and 1 could be found.

The elastic energy of the different conformation at given z and n can be computed with the following biphasic expansion of the elastic energy

$$E(\kappa_\pm, \tau_\pm, \alpha) = \alpha L \varepsilon_+ + (1-\alpha) L \varepsilon_- \tag{12}$$

Notice that a decomposition of the elastic energy into two unlike handedness terms has been invoked by Goldstein et al. (2000) in the context of bistable helices. In the Kirchhoff model, linear densities of energy $\varepsilon_\pm$ write

$$\varepsilon_\pm = \frac{1}{2} B (\kappa_\pm - \kappa_0)^2 + \frac{1}{2} C (\tau_\pm - \tau_0)^2 \tag{13}$$

The elastic energies of all three state-namely the pure (+)-green- or (−)-blue- states and the mixed state (+/−) -red- when it exists are depicted in fig. 6(c) as a function of the number of turns. We see that when the mixed state exists, its total energy is found to be lower than the energies of both pure states at the corresponding n and z. The mixed state then provides a convexification of the energy of the system as shown in fig. 7. Therefore, when $\alpha = 0^+$ and 1^-, the system is expected to adopt the state of lowest energy, that is the mixed state. Indeed, we see in fig. 5, that the red curve predicted by the biphasic model fairly well coincides with the experimental domain of existence of the mixed state.

At a given z and n, solving the system of equations (9) and (11) allows us to express the axial force and torque in the coexisting regime, when it prevails. When it is not the case, the axial force and torque can also be expressed in

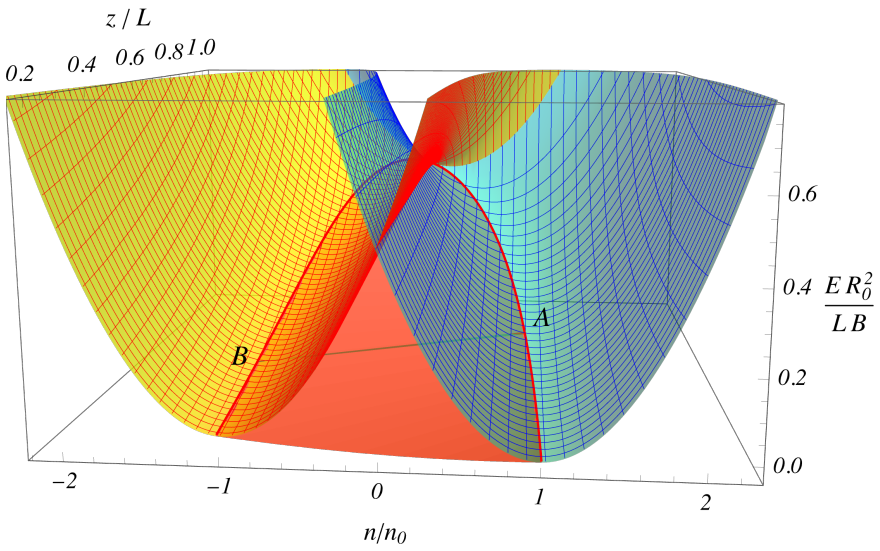

Figure 7: Calculations in biphasic model. Elastic energy of pure helices with positive (blue) and negative (yellow) chiralities, drawn as a function of the system extension z/L and winding ratio n/n_0. A typical two-well profile emerges, and for a region of z and n values, the energy of the system can be made convex by considering a mixed phase (red surface) joining the two wells in a tangent manner along the red curve. Point A is such that $n/n_0 \simeq 0.91$, $z/L \simeq 0.6$, $\frac{E_\kappa R_0}{B} \simeq 0.06$. Point B is such that $n/n_0 \simeq -0.97$, $z/L \simeq 0.36$, $\frac{E_\kappa R_0}{B} \simeq 0.09$. Fixed parameters are $z_0/L = 0.2$ and $\Gamma = 2/3$.

the pure states (+) or (−) by solving the same system of equations for $\alpha = 1$ and $\alpha = 0$, respectively. The obtained curves for axial torque and force at a given n as a function of z are plotted in fig. 3 alongside the experimental data. Consistently, the model predicts two regimes: at low values of z, the axial torque and force correspond to the coexisting regime, with a slope discontinuity observed at the disappearance of the perversion. The second regime corresponds to the pure state—above the red line in fig.5. The predicted curves for axial force and torque based on the biphasic model are also plotted for values of z/L between 0.5 and 1 and for values of n/n_0 between −1 and 1 in fig.4(c) and (d). The red line represents the axial torque and force at the domain limit where the (+/−) state exists. In fig. 4(c), it is clearly visible that during the migration of the perversion, in the coexistence regime, the variations in axial torque are smaller than those in the pure state. It can also be shown that for low z_0/L and high extension $z/L \lesssim 1$, the overall variation in axial torque during perversion migration is negligible compared to the magnitude of the axial torque itself. During coexistence, the axial torque M and the axial force T vary with n, though the variation of M is small (Dilly et al., 2023, fig. 2). Useful approximate relations of the torque plateau value and its variation can be found in the present biphasic approach. Generalizing eq (A.3) to $z/L < 1$, the average value of the plateau is seen to approximately follow

$$M_{\text{plateau}} \equiv M(n=0) \approx -\Gamma \frac{B}{R_0} (z/L)(z_0/L) \sqrt{1-(z_0/L)^2} \tag{14}$$

The plateau itself is slightly concave and increasing with n and its variation within the mixed phase can be approximated as

$$\Delta M \equiv M(\alpha = 1^-) - M(\alpha = 0^+) \approx 2.5\,\Gamma \frac{B}{R_0} (1 - z/L)(z_0/L)^2 \tag{15}$$

These formula are compared to numerical values in fig. 8. We see that M_{plateau} increases with z/L and z_0/L and that as $z \to L$, the torque plateau gets flat.

It is in fact possible to have rigorously constant values of M and T during the transition. As the system enters the coexistence region, $\alpha = 1$ and the values of the curvatures and torsions for both phases are determined, for example for point A in fig. 8 we have $\kappa^+ = 0.71/R_0$, $\kappa^- = 0.89/R_0$, $\tau^+ = 0.53/R_0$, $\tau^- = -0.34/R_0$, $T = 0.37\,B/R_0^2$, and $M = -0.06\,B/R_0$. Inserting these values in system (11), we see that z and n now both linearly depend on α, and if we follow this line $(z(\alpha), n(\alpha))$ as α varies from 0 to 1 (for example from point A to point B in fig. 8) all the variables of

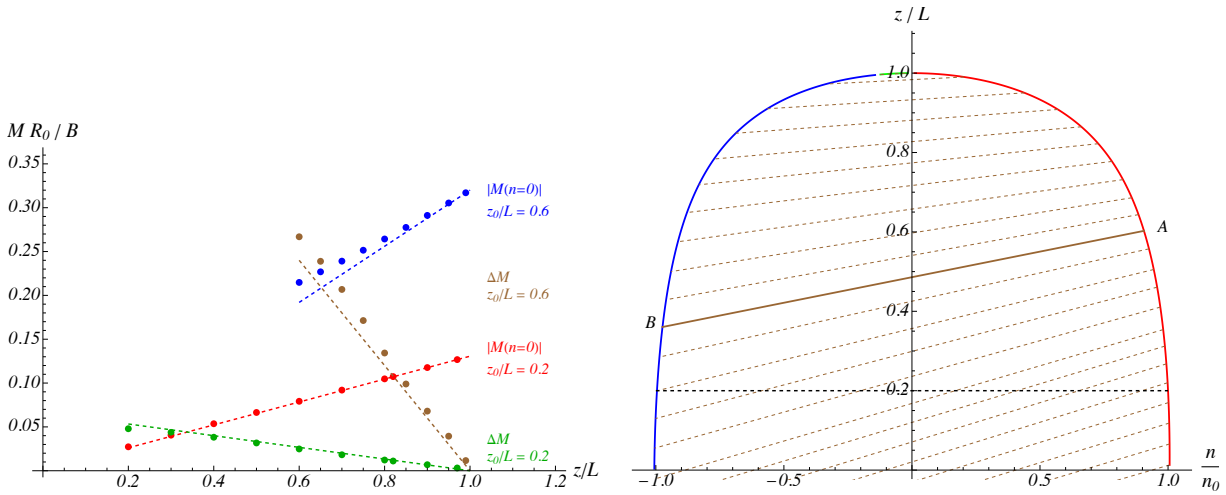

Figure 8: Biphasic model calculations. (Left) Blue and red: Axial torque at zero number of turns ($n = 0$) as a function of z for $z_0/L = 0.6$ (blue) and 0.2 (red). We also plot in brown ($z_0/L = 0.6$) and green ($z_0/L = 0.2$) the difference in axial torque values between the injection and expulsion of the perversion, associated to the deviation of the axial torque from its plateau value, as defined in eq. (15). Dots correspond to results of the biphasic model while dashed lines correspond to the analytical results obtained in eq. (14) for the axial torque and eq. (15) for the deviation of the axial torque. (Right) Limits for the coexistence region in the case where $z_0/L = 0.2$. Red curve: domain limit with pure (+) helices, blue and green lines: limit with pure (−) helices. Brown straight lines: (dashed and solid) trajectories where the axial force and torque are rigorously constant. On the solid brown line, point A is such that $n/n_0 \simeq 0.91$, $z/L \simeq 0.6$ and point B is such that $n/n_0 \simeq -0.97$, $z/L \simeq 0.36$. Transition trajectories within green portion connect two helices of the mixed state with same (−) chiralities. Fixed parameter: $\Gamma = 2/3$.

the system (curvatures, torsions, axial torque and force) stay rigorously constant. We draw lines of constant torque and force for different transitions in figure 8. These lines are trajectories in the (n, z) space where the axial torque and force imposed to the mixed state (+/-) are constant, the only varying quantity being the proportion of phases (+) or (-), analog to the pressure-temperature diagram in liquid-gas transition.

3.3. Neglecting boundaries: shooting along the heteroclinic connection and perversion solution

In the biphasic model, we suppose that the connection between the two helices exist but we neglect its participation to the energy of the system. We also suppose that α is free to vary in order to satisfy the conservation of the Kirchhoff integrals (7) and the boundary conditions. But it is not clear, on the one hand, whether the connection does in fact exist and, on the other hand, that the connection indeed allows for the free variation of the parameter α. Following the shooting approach of Champneys and Thompson (1996) to identify solutions to the Kirchhoff equations that connect specific boundary conditions, which was later applied by McMillen and Goriely (2002) to explore connections between symmetric helices of opposite chiralities, we extend the analysis to determine the heteroclinic connection between two asymmetric helical solutions in the presence of intrinsic torsion. Our results show that this connection (the perversion solution) does not always exist within the set of connectable helices.

3.3.1. Numerical shooting method

In fig. 6(b), the (red) curve corresponds to helical states that can be connected by a perversion. To find the shape of the perversion, we numerically solve the Kirchhoff equations, subject to boundary conditions, using the shooting technique described by McMillen and Goriely (2002). Defining $\mathbf{X} = (T_1, T_2, T_3, \kappa_1, \kappa_2, \kappa_3)^{\mathrm{T}}$, we write eq. 6 under the

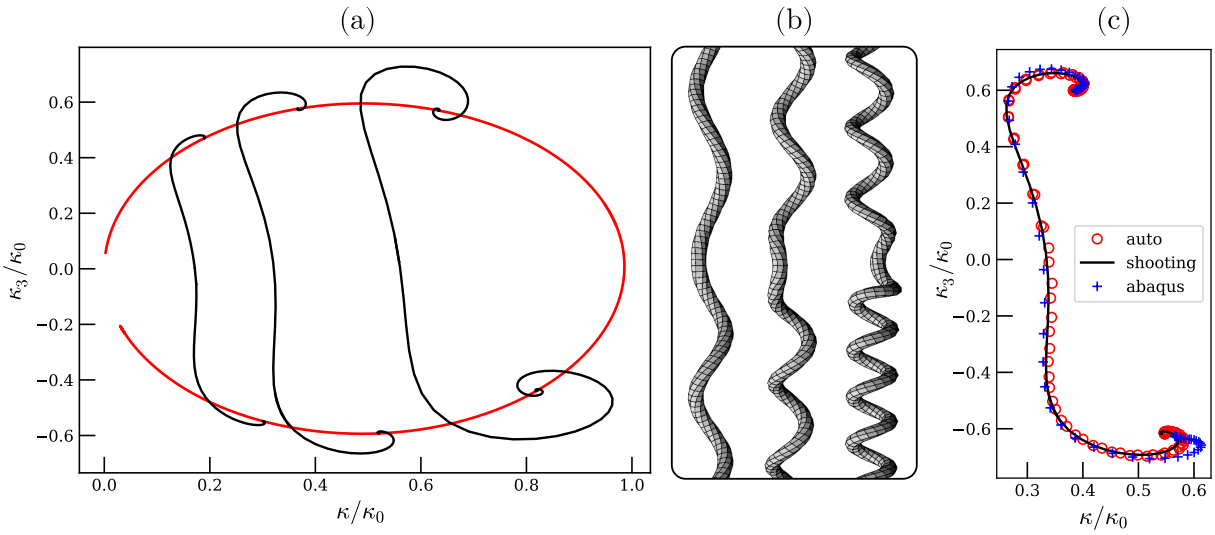

Figure 9: (a) Perversion solutions -black line - in the $\left(\kappa = \sqrt{\kappa_1^2 + \kappa_2^2}, \kappa_3\right)$ space connecting two helices on the curve of connectable helices - red line-, for $\Gamma = 2/3$ and $z_0/L = 0.3$. Solutions are obtained with the shooting technique described in section 3.3. From left to right, the solutions corresponds to axial forces $T/\left(B\kappa_0^2\right) = 1.17, 0.90$ and 0.51. (b) Same solutions in spatial coordinates. (c) Comparison of the perversion solution in the (κ, κ_3) space obtained with ABAQUS 3D finite element simulation, the shooting method, and AUTO simulations (see section 3.4), for $z_0/L = 0.2$ at $z/L = 0.82$ and $n/n_0 = 0$. ABAQUS simulations were carried out with a Poisson ratio $\nu = 0.49$, $n_0 = 5$ and $R_0 = 3.9$ mm.

form

$$\mathbf{X}' = \mathbf{F}(\mathbf{X}) \tag{16}$$

where $\mathbf{F}$ is a 6-dimensional non-linear function of $\mathbf{X}$. Helical states correspond to fixed points of (16), that is, uniform solutions to the Kirchhoff equations, $\mathbf{F}(\mathbf{X}_\pm) = 0$. As described above, the helical solutions in the coexisting state take the form $\mathbf{X}_\pm = (\gamma_\pm \tau_\pm \kappa_\pm, 0, \gamma_\pm \tau_\pm^2, \kappa_\pm, 0, \tau_\pm)$, where κ_+, τ_+ (resp. κ_-, τ_-) are the curvature and torsion of a helix with positive (resp. negative) chirality. Finding the perversion solution implies finding the trajectory, called a heteroclinic connection, of the equivalent dynamical system (16) between two fixed points $\mathbf{X}_+$ and $\mathbf{X}_-$. To find this connection, we have to numerically compute the trajectory that starts on the unstable manifold of the first point, say $\mathbf{X}_+$, and ends on the stable manifold of the other point, say $\mathbf{X}_-$. The six eigenvalues of the Jacobian of $\mathbf{F}$, for instance at the fixed point $\mathbf{X}_+$, are numerically computed and are of the form $(0,\ 0,\ \sigma_+ + i\omega_+,\ \sigma_+ - i\omega_+,\ \sigma_- - i\omega_-,\ \sigma_- + i\omega_-)$, where $\sigma_+ > 0$ and $\sigma_- < 0$. We see that two of these eigenvalues are zero and four are complex. The subspace defined by the eigenvectors corresponding to eigenvalues with positive real part yields the direction in which the helix is unstable, and corresponds to an unstable manifold of dimension 2. The shooting technique therefore consists of shooting in this two-dimensional subspace and tuning the direction so that the trajectory converges towards the (stable manifold of the) other connected fixed point, thereby yielding the heteroclinic orbit. In practice, we shoot around both the fixed points $\mathbf{X}_-$ and $\mathbf{X}_+$, and tune the direction on the unstable manifolds so that the two trajectories connect. We therefore place one initial point on the unstable manifold of the fixed point $\mathbf{X}_+$, with eigenvector $\mathbf{v}_+^{(u)}$ and we set our initial condition as

$$\mathbf{X}(0) = \mathbf{X}_+ + \epsilon \left[\mathcal{R}e\left(\mathbf{v}_+^{(u)}\right)\cos(\theta) + \mathcal{I}m\left(\mathbf{v}_+^{(u)}\right)\sin(\theta)\right], \tag{17}$$

with ϵ small (10^{-4}) so that the initial condition lies close to the fixed point. The trajectory is then numerically computed with an ODE integrator for different directions θ_+. We perform the same integration around point $\mathbf{X}_-$ for different directions θ_- and find that, for a unique couple of direction (θ_+, θ_-) the two trajectories connect and form a heteroclinic orbit. Several example of these heteroclinic trajectories are displayed in fig. 9(a) in the $\left(\sqrt{\kappa_1^2 + \kappa_2^2}, \kappa_3\right)$ projection, each corresponding to different couple of helices with different axial torques and forces. They connect helices of positive chiralities to helices of negative chiralities. The solution is reconstructed in spatial coordinates in

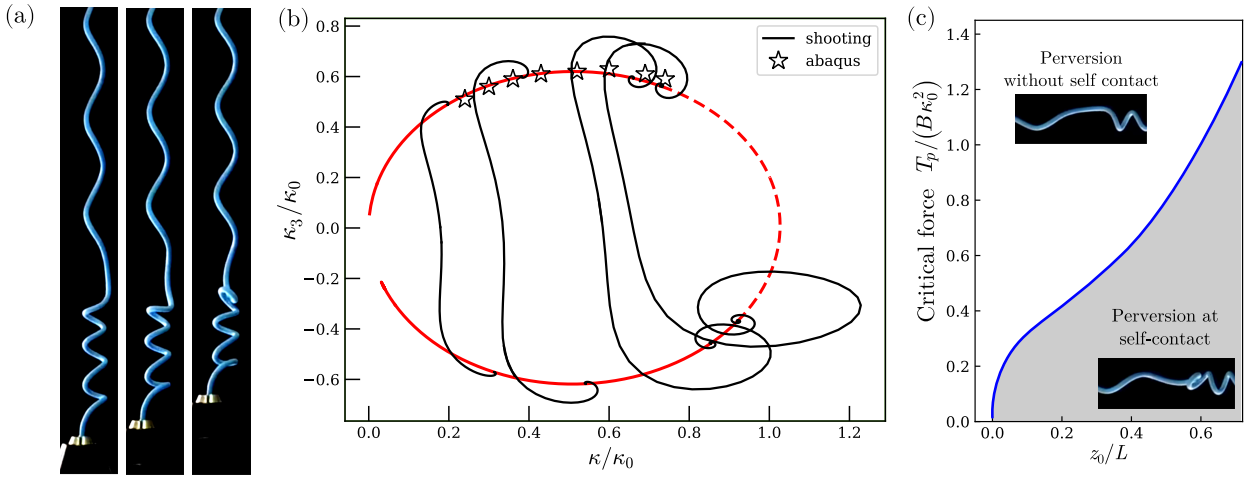

Figure 10: (a) Perversion jumping to self-contact for decreasing extension. For a given n, as z is decreased, the perversion becomes unstable at a critical z. (b) Black line: perversion solutions obtained with the shooting method for $\Gamma = 2/3$, $z_0/L = 0.2$ and a range of forces - from left to right - $T/\left(B\kappa_0^2\right) = 1.11,\ 0.84,\ 0.48$ and 0.41. Full red line: helices connectable by perversion. Dashed red line: no perversion solution could be found by shooting method. White stars: κ and τ of the (+) helix of the coexisting state found by the ABAQUS simulations. No stable $(+/-)$ solution could be found by ABAQUS for curvatures higher than $\kappa = 0.74\kappa_0$ (the last star). (c) Numerical phase diagram of existence of perversion solutions without self contact for $\Gamma = 2/3$. Below the critical force T_p the non self touching perversion does not exist and corresponds to the conformation on the dash-dotted part of the curve of connectable helices shown in panel (b) at the given z_0.

fig. 9(b). For low values of the axial force, on the far right of the curve of connected helices in fig. 9(a), the heteroclinic trajectory (i.e. the perversion solution) could not be found. It is the subject of the next section.

3.3.2. Heteroclinic collapse and jump to self contact

The biphasic model described in 3.2 assumes a connection between two helices of opposite chirality, but this is not always the case. In experiments, as the extension z (or axial force T) is decreased, the perversion can lose stability. Such an experiment is displayed in fig. 10(a): starting at a given n in the coexistence zone, where the system is in a mixed $(+/-)$ state, while decreasing z, the perversion destabilizes at a critical z value where the rod jumps (or snaps) towards self-contact. From the theoretical point of view, as we span the (red) curve of possible connected helices of fig. 9(a) from left to right, the axial force T and extension z of the system decreases, while κ_+ increases. At a critical point along the red curve, perversion solutions can no longer be found. Fig. 10(b) shows several perversion solutions connecting helices on the solid red curve in the (κ, κ_3) space, with $\kappa^2 = \kappa_1^2 + \kappa_2^2$. As the solid red curve becomes dashed, the critical point is crossed: no perversion solutions exist for high values of κ_+ or, equivalently, low values of the axial force or extension. For this critical helix couple, $(\kappa_+^c, \tau_+^c, \kappa_-^c, \tau_-^c)$, the critical values of the axial torque M_p and the axial force T_p are given by eq. (9). Using eq. (11), we see that in the (z, n) space this critical transition where the perversion solution disappears is a straight line, plotted in blue in fig. 5. Above this line, perversion solutions are found while below it, perversion solutions cannot be found. We note that in the unwinding experiments presented in fig. 2, at low z values (for example $z/L < 0.6$), the mixed state had self-contact. Nevertheless, as n was decreased under a critical value, self-contact was removed. This critical n value depends on z/L and is plotted with blue diamonds in fig. 5. These blue diamonds approximately agree with the destabilization (blue) line corresponding to the disappearance of the perversion solution.

The experiment depicted in fig. 10(a) was also simulated using the finite element method (FEM). We choose the static implicit scheme of ABAQUS® with 3D elements and a hexagonal mesh. We use a rod with a helical rest shape

having 5 coils, $z_0/L = 0.2$, and Poisson ratio $\nu = 0.49$. As the nucleation of the perversion is generally associated with a jump, see for example fig. 11, we can not simply decrease n in the static scheme of ABAQUS but rather have to rely on a carefully-chosen sequence of rotations of the clamps to induce the perversion continuously. Examples of such a manipulation can be seen in Supplemental Material (Dilly et al., 2024, videos 4 and 5). Once the perversion is generated and the clamps are approximately realigned, we decrease n to ($n = -0.09\ n_0$) so that the perversion does not lie near the clamps. By axial translation of one of the clamps, the translation experiment presented in fig. 3 is numerically reproduced. One of the obtained solutions is plotted in fig. 9(c), for $n/n_0 = -0.09$ and $z/L = 0.82$ with $z_0/L = 0.2$, linking approximately the same helices as for $n/n_0 = 0$ and $z/L = 0.82$. We see a good agreement with the results from the shooting method for the perversion solution. The extension z/L is subsequently decreased and we plot by stars the values of κ_+ in the (+) helix obtained in ABAQUS for different extensions in fig. 10(b) - for the sake of clarity the whole perversion solution is not plotted. At a critical z (or κ_+) value, ABAQUS failed to converge toward a regular solution, indicating a jump to a configuration with self-contact. This critical event corresponds to the last star in the diagram, which agrees well with the critical value found via the shooting technique.

The critical force T_1 at which the perversion destabilizes was subsequently computed using the shooting technique for different values of intrinsic extension z_0/L, and the resulting curve is plotted in fig. 10(c). We see that the critical force T_1 of perversion destabilization increases as the unloaded helix extension z_0 increases. We also observed that the process of perversion collapse towards self-contact is not reversible and exhibits hysteresis. Starting in the white area in fig. 10(c) and decreasing the applied tension, the perversion collapses into self-contact when the blue line is crossed and as the system enters the gray area. If the applied tension is then increased again, the perversion remains stuck in the self-contact configuration, even when the system returns to the white area. This indicates that destabilizing the self-contact configuration requires a higher force than the one that initially induces the collapse into self-contact, see Supplemental Material (Dilly et al., 2024, video 6).

We also note that below the blue line in fig. 5, where conformations have a perversion with self-contact and thus involves friction within the rod. In these cases it becomes unclear and it seems difficult to assume that the proportion of helices, α, is free to vary. Consequently, the lower part of the diagram in fig. 5 lies outside the scope of the biphasic model.

To summarize, theoretical approaches that account for the perversion agree on the fact that the gray shaded area between the red and blue lines in fig. 5 represents the domain of existence for the mixed state (+/−), with a perversion with no self-contact. Supplementary effects, such as finite size effects at the boundaries, can also be accounted for through numerical simulations and this is the subject of the next section.

3.4. Taking into account boundaries and perversion: Numerical simulations with AUTO

In this section, we show how we numerically compute the equilibrium of the rod as it is clamped at both ends. The precise boundary conditions

$$\mathbf{r}(s=0) = (0,0,0)\,, \quad \mathbf{d_1}(0) = (1,0,0)\,, \quad \mathbf{d_2}(0) = (0,1,0)\,, \quad \mathbf{d_3}(0) = (0,0,1) \tag{18a}$$

$$\mathbf{r}(s=L) = (0,0,z)\,, \quad \mathbf{d_1}(L) = (\cos\beta, \sin\beta, 0)\,, \quad \mathbf{d_2}(L) = (-\sin\beta, \cos\beta, 0)\,, \quad \mathbf{d_3}(L) = (0,0,1) \tag{18b}$$

are here taken into account and the differential system (1), (2), (3) together with (18) define a well-posed boundary-value problem. We manipulate non-dimensionalized forces $\hat{\mathbf{T}} = \frac{\mathbf{T}L^2}{B}$, moments $\hat{\mathbf{M}} = \frac{\mathbf{M}L}{B}$, curvatures $\hat{\boldsymbol{\kappa}} = \boldsymbol{\kappa}L$, positions $\hat{\mathbf{r}} = \frac{\mathbf{r}}{L}$. Consequently the set of free parameter comprises $\Gamma = C/B$, n_0, z_0, and the applied translational Δ and rotational β displacements.

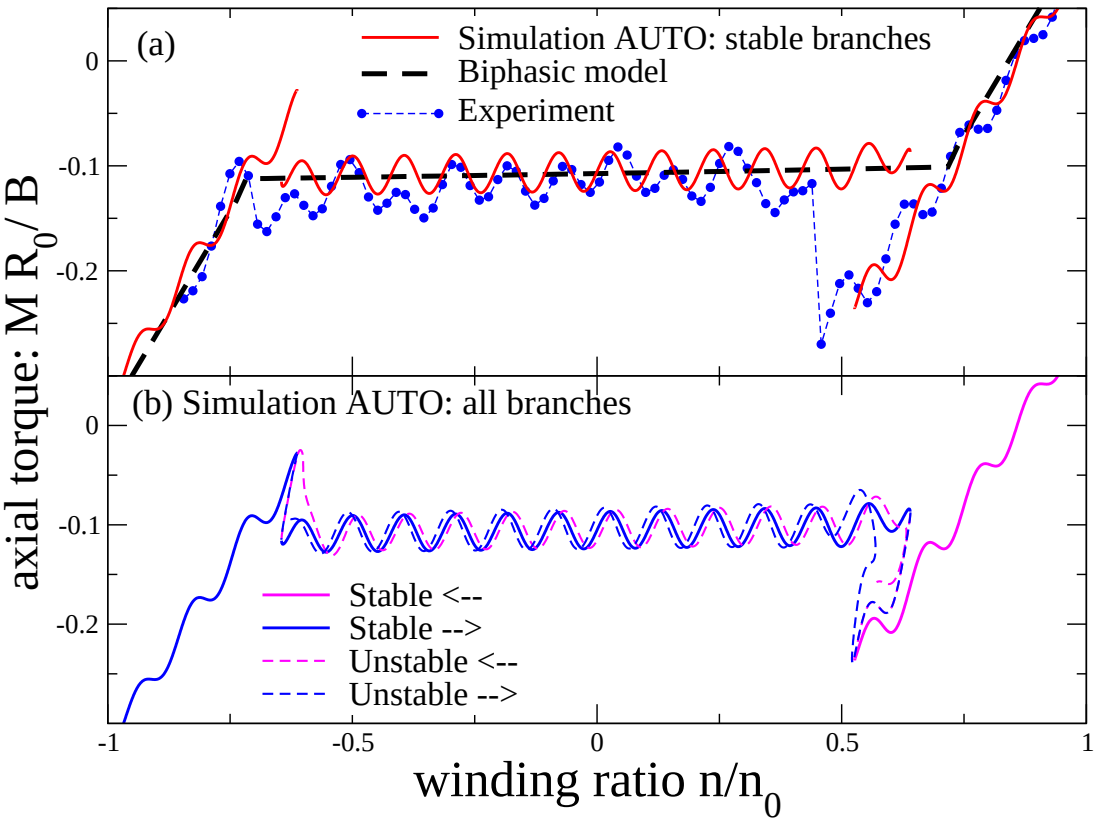

Figure 11: Axial torque M for a clamped helical rod as the winding ratio n/n_0 is varied. (a) Experimental data, the biphasic approximation, and the numerical simulation using AUTO (stable branches only) (reproduction from Dilly et al. (2023)). (b) All branches computed using AUTO: solid violet (unwinding, stable), dashed violet (unwinding, unstable), solid blue (winding, stable) and dashed blue (winding, unstable). Fixed parameters: $\Gamma = 2/3$, $n_0 = 9.5$, and $z/L = 0.82$.

In addition, three global quantities are important to characterize an equilibrium solution: the total twist Tw, the writhe Wr, and the link $Lk = n$. The total twist has a simple definition

$$Tw = \frac{1}{2\pi} \int_0^L \kappa_3 \, \mathrm{d}s \tag{19}$$

The writhe and the link are usually only defined for closed curves, but they can be generalized to the present case of a clamped-clamped rod (Berger and Prior, 2006). The writhe is a property of the center line $\mathbf{r}(s)$ only and measures how this center line is curled. In principle, it is defined in the following way. We look at the rod from a direction in space, project its shape onto an imaginary screen perpendicular to the viewing direction and count the number of (signed) self-intersections one sees on the projected shape. The procedure is repeated for all viewing directions uniformly distributed over the unit sphere, and the writhe is the mean number of the self-intersections Fuller (1971); Aldinger et al. (1995). In practice, we use the fast algorithm introduced by Berger and Prior (2006) to compute the polar writhe, see also (Prior and Neukirch, 2016). The link is the total number $Lk = n$ of rotation turns which have been applied to the system. A value $Lk = 0$ corresponds to a geometric configuration that is straight and untwisted. By geometric configuration, we mean a configuration which is kinematically admissible (i.e. satisfies the boundary conditions) but not necessarily statically admissible (it does not have to be an equilibrium configuration). The long way to compute the link of an equilibrium configuration is then to first pull it straight and then rotate its ends to completely remove the twist, the total rotation turns needed to do so being the link of the equilibrium configuration. We stress that, during this kinematic straightening and unwinding process, no self-crossing of the center line of the rod should happen. An important relation between the three quantities is

$$Lk = Tw + Wr \tag{20}$$

as shown by Călugăreanu (1959) and Fuller (1978). In our present clamped-clamped scenario, we have $\beta/(2\pi) = Lk \, mod \, 1$, or said differently we always know the decimal part of the link, but we have to keep track of its integer part, either by continuation or by computing the (polar) writhe and use eq. (20). Practically, we compute a precise value of the link by using an approximate value $Lk_{\text{approx.}}$ coming from the previous point on the continuation branch or from a quick (i.e. with a reduced number of discretization points) computation of the polar writhe. Once $Lk_{\text{approx.}}$ and β are known, the precise value of the link is given by

$$Lk = \frac{\beta}{2\pi} + \text{Round}\left(Lk_{\text{approx.}} - \frac{\beta}{2\pi}\right) \tag{21}$$

where $\text{Round}(x)$ is the integer nearest to the real number x.

The present approach only computes equilibrium solutions and does not treat self-contact. We use the Fortran/C library AUTO07p to solve the boundary value problem, see (Doedel et al., 1991). This library uses orthogonal collocation to discretize the strong form (1), (2), (3) of the equilibrium equations with Lagrange polynomials of degree NCOL=3 to 7 and NTST segments. A Newton-Chord method is then called to solve the obtained nonlinear algebraic problem where the Jacobian is computed through numerical differentiation. Once a solution is known for a given value of the parameters, a pseudo-arclength continuation approach is used to vary one of them. It took a MAC M1 ARM with 8 CPU cores (AUTO uses OPENMP) roughly half a minute to compute the 3650 points along each branch (NCOL=5, NTST=70). The full solution (shape, force, moment, curvatures) is stored only for a dozen of points along each branch, leading to a few MB of disk space for the full diagram.

The resulting bifurcation diagram for fixed $z_0/L = 0.2$, $n_0 = 9.5$, $z/L = 0.82$, $\Gamma = 2/3$ (i.e. $\nu = 1/2$) and varied number of turns $n = Lk$ is shown in fig. 11(b). We added a small amount of self-weight in z-direction as an imperfection parameter to ease the numerical computations. The diagram comprises two branches, the first has been computed by starting with a positive value of the number of turns: $n \approx 1.5\, n_0$, while the second has been computed by starting with a negative value, $n \approx -1.5\, n_0$. Each branch contains stable and unstable equilibrium solutions and in an actual experiment jumps (snaps) would happen. The torque plateau value is found in accordance with the biphasic

approach with undulations due the length phase between the location of the perversion and the clamps. Please also note that the stable part of the first and second branches have the same (torque, winding ratio) profile but that they correspond to different solutions as the perversion is not located at the same position in each of the branches, the asymmetry coming from the imperfection due to the self-weight.

Notice that both branches have a sub-critical bifurcation corresponding to the injection of the perversion, either from above (unwinding) or from below (winding). Over a range of n near injection/expulsion three branches are present: two stable and one unstable. According to the arguments of first-order transitions, upon unwinding, the system keeps its stable configuration as long as the stable branch exists and jumps to the second stable branch when the first one disappears. These jump sizes seen in the numerics are in accordance with the experimental findings: as n is decreased, a large jump at perversion injection and a small jump when the perversion is expelled, see fig. 11.

We also use the AUTO simulation to compute the transition at which the perversion solution breaks down giving way to self-contact. Points in (n, z) space at which the perversion solution destabilizes are plotted as black circles in fig. 5. For points away from the red curve, we observe a very good agreement between these values and the values obtained with the shooting method approach (blue line), see section 3.3.2. For points close to the red curve, the AUTO simulation differs from the shooting approach because the latter assumes an infinite system and therefore neglects finite size effects, i.e. the effects of the clamps.

3.5. Comparison of the different theories

To illustrate the differences between the methods used in this section, we plot in fig. 12 a comparison between the perversion solutions obtained using the biphasic model, the shooting approximation, and AUTO. Left panel shows the profiles of the three components of the curvature $\kappa_1(s)$, $\kappa_2(s)$, $\kappa_3(s)$ and the force $F_1(s)$, $F_2(s)$, and $F_3(s)$. All are solutions of eqs. (1), (2), (3), (4), but using different assumptions. The resulting energy density is also given and one sees that the shooting method regularizes the artificial energy jump of the biphasic model at the perversion. In addition, the full AUTO computation takes into account the clamps, therefore adapting the profiles to the precise boundary conditions. The right panel shows the corresponding profiles together with the experimental one. Notice that the shooting method reproduces, in a very satisfactory way, the perversion profile.

4. The case $n = 0$: The writhing transition

On the particular line $n = 0$ in the phase diagram in fig. 5, when $z/L = 1 - \varepsilon$, as $\varepsilon \to 0$, the system undergoes the writhing transition. As derived by McMillen and Goriely (2002) for a helical rod with no intrinsic torsion ($z_0 = 0$), starting from $z = 1$ and decreasing the imposed axial force T , the straight rod becomes unstable for at the critical value

$$T_c = B\kappa_0^2/\Gamma\,, \quad M_c = 0 \tag{22}$$

Upon a pitchfork bifurcation (Strogatz, 1994) two symmetric helices of opposite chiralities appear, connected by a perversion. It is interesting to note that the critical force at which writhing occurs at $n = 0$ remains the same in the presence of intrinsic torsion, or equivalently intrinsic extension z_0 (Dilly et al., 2023). The aim of this section is to report our experiments on the writhing transition on the particular line $n = 0$ for a rod of negligible intrinsic torsion compared to its intrinsic curvature, that is, in the multi-circle limit. The loading force and curvature at the writhing transition were measured and compared to theoretical predictions of McMillen and Goriely (2002) and Dilly et al. (2023).

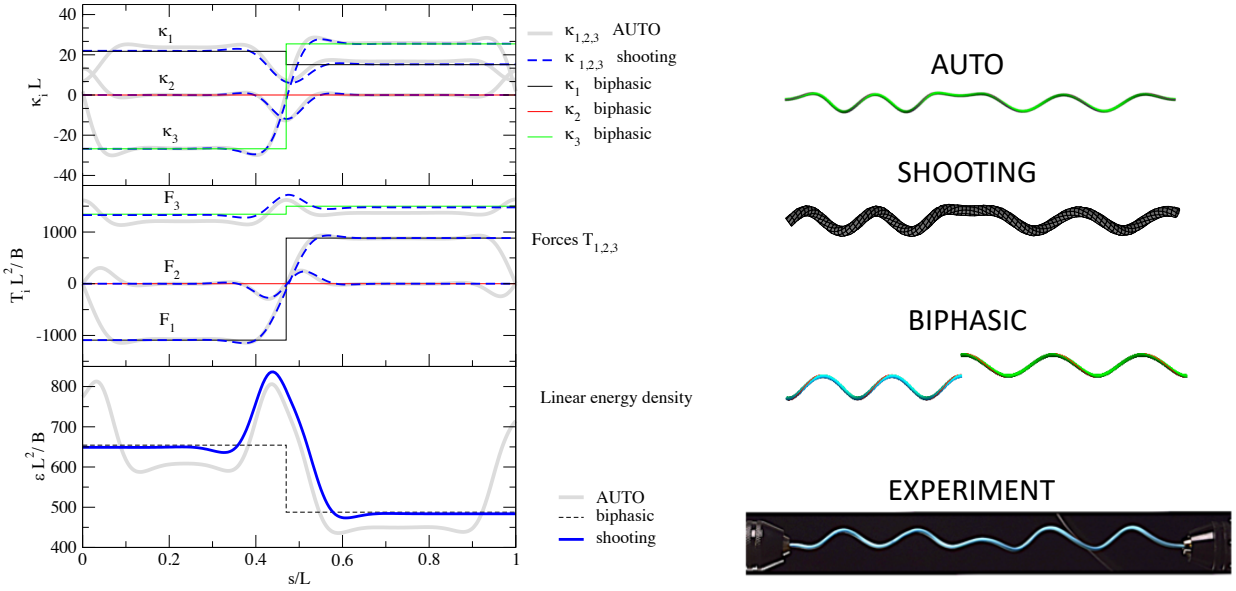

Figure 12: The upper left panel presents the three curvature components obtained with AUTO simulation - gray -, with the shooting method - dashed - and in the biphasic model -colored -. With the same drawing conventions, the middle left panel presents the force vector components and the lower left panel presents the elastic energy per unit of arclength. The right part of the figure shows the system configuration computed with the three different numerical techniques and the corresponding experimental one. Fixed parameters are $z_0/L = 0.2$, $z/L = 0.82$, $n_0 = 7$, $\Gamma = 2/3$.

4.1. Experiments

Fig. 13(a) displays snapshots of an experiment of the writhing transition, see also Supplemental Material (Dilly et al., 2024, video 2). A helical rod of radius $R_0 = 4.2$ mm was made as described in section 2.1, with pitch and thickness equal to $P_0 = d = 1.8$ mm. At rest the coils were nearly in contact, that is the natural helix was as close as possible to the multi-circle configuration. These values of intrinsic radius and pitch lead to intrinsic curvature and torsion: $\kappa_0 = 2.4\times10^2$ m^{-1} and $\tau_0 = 1.6\times10^1$ m^{-1}, and therefore, $\tau_0 \ll \kappa_0$. The rod was clamped at both extremities in mandrels, see fig. 1(a), in such a way that the tangent vector of the center-line of the rod was vertically aligned at both ends of the rod. A red line was drawn on the exterior of the rod when it was at rest and once clamped and straightened, one extremity was rotated so that the red line became straight, setting $n = 0$. The initial extension was set to $z > 1$ taking advantage of the extensibility of the rod, and the axial force T was monitored upon decreasing the distance z between the two mandrels. For a given z (or equivalently T) value, two helices of opposite chiralities appear, connected by a perversion. A typical force-extension profile is shown in fig. 14. The biphasic model presented in section 3.2 predicted that, at $n = 0$, for any $z/L < 1$, coexisting helices appear. However, in our model values $z/L > 1$ are inaccessible due to the assumed inextensibility of the rod. In the experiment, the rod has extensibility and values of $z/L > 1$ are in fact accessible. Nonetheless, in the force-extension profile presented in fig. 14, two distinct regimes are observed, marked by a noticeable change in slope between them. For large extensions, the axial force decreases steeply as the rod's extension decreases. At the onset of the writhing instability, and during the formation of the pair of helices with opposite chiralities, the slope of the axial force decreases. In fig. 14, the slope change is clearly visible and this transition in axial force behavior defines a critical writhing force above which the rod remains straight and the axial stiffness is primarily governed by the rod's extensibility. Below this critical force, however, the axial stiffness of the rod is determined by the extension of a pair of helical Kirchhoff rods, where the effects of extensibility are relatively small.

Curvature and torsion in the helix of positive chirality were measured through a stereoscopy method presented in

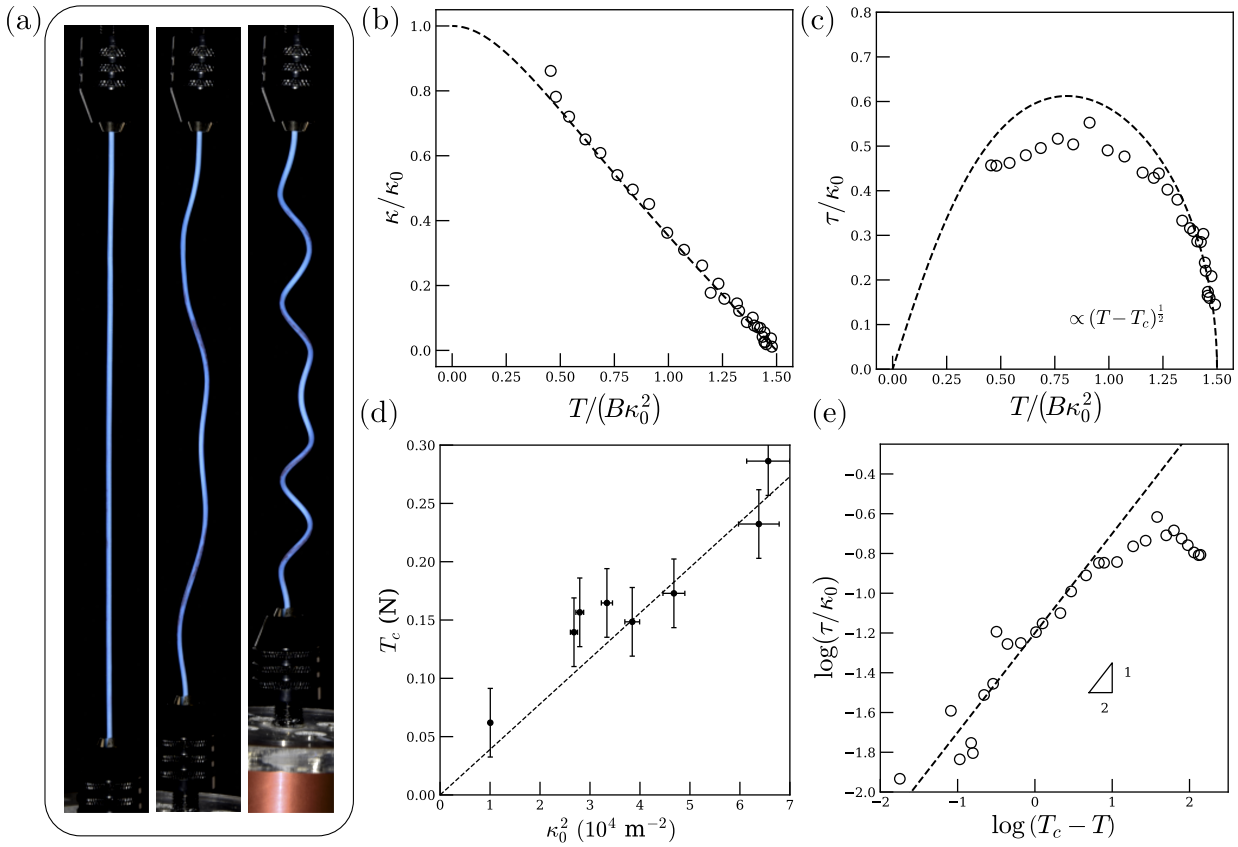

Figure 13: (a) Snapshot of the writhing experiment. A helical coil with $\tau_0 \ll \kappa_0$ (equivalently $z_0 \ll 1$ as the rod has negligible intrinsic extension) is unwound so that the number of coils of the mixed state is 0. At its maximal extension, the rod is straight. As extension is reduced, two helical coils appear, linked by a perversion. (b) Curvature as a function of the axial force during the writhing experiment. Dashed line: linear fit on the bending rigidity B of the expected axial force for a Kirchhoff rod with zero intrinsic torsion and twist-to-bend ratio $\Gamma = 2/3$. (c) Circles: Experimental torsion as a function of normalized axial force obtained in (b). Dashed line corresponds to the expected torsion of a Kirchhoff rod with zero intrinsic torsion. (d) Critical force of the writhing instability of different elastomeric rods having different intrinsic curvatures, as a function of the square of the intrinsic curvature. Dashed line: expected curve for the writhing critical tension, without fitting parameter taking $B = 2.4 \times 10^{-6}$ Pa·m^4 and $\Gamma = 2/3$. (e) Log-log plot of torsion as a function of axial force. Dashed line: line of slope $1/2$. Fixed parameters: $\Gamma = 2/3$, $z_0/L = 0$.

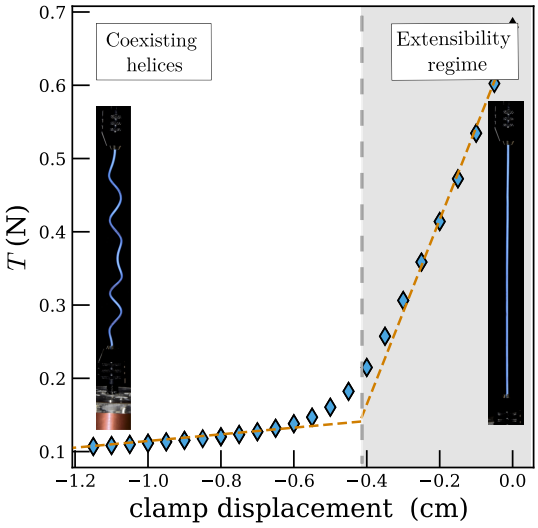

Figure 14: Axial force T as a function of axial displacement during the writhing experiment for a rod with an intrinsic radius $R_0 = 6.1$, number of coils at rest $n_0 = 8.75$, pitch $P_0 = 1.8$ mm, and cross-section diameter $h = P_0 = 1.8$ mm.

Appendix B and are plotted on fig. 13(b) and (c), as a function of the axial force. Consistently with observations, these curvature and axial force measurements reveal that for large force values the rod is straight and at a critical axial force, the curvature in the helices (or equivalently the radii of the helices) increases. In this experiment, the critical force for writhing was estimated by performing a linear fit on the curvature values as a function of the applied force. The critical force was defined as the zero of the linear fit, corresponding to the force value at which the curvature vanishes. Measurements of torsion reveal that, at the critical force of writhing, torsion increases steeply. Then, as the force is further decreased, the torsion in the helix decreases. The steep variation of torsion as a function of the axial force is highlighted in the log-log plot in fig. 13(e). Around the critical force of writhing, the torsion is evidenced to scale as the square root of the distance to the writhing instability in terms of axial force.

The writhing experiment was also performed for helices with different radii, all having the same pitch $P_0 = 1.8$ mm. The corresponding critical forces T_c were determined from the force-extension profiles, fig. 14, as described above. The measured values of the writhing critical force T_c as a function of the intrinsic curvature κ_0 are plotted in fig. 13(d), indicating a quadratic dependence of T_c with κ_0, as shown by McMillen and Goriely (2002) and retrieved in our model.

4.2. Theory

As the intrinsic torsion in the experiments presented above is small compared to the intrinsic curvature, we study the system presented in section 3.2 in the limit $\tau_0 \to 0$, or equivalently, in the limit $z_0/L \to 0$. In this limit, the rod natural shape is circular and the system of eq. (9) reduces to a unique equation:

$$(\kappa - \kappa_0)\,\kappa + \Gamma\,\tau^2 = 0 \tag{23}$$

where the curvature and torsion of the positive helix are $(\kappa_+, \tau_+) = (\kappa, \tau)$, and of the negative helix are $(\kappa_-, \tau_-) = (\kappa, -\tau)$. The connected helices are symmetric and their curvature and torsion lie on the ellipse given by eq. (23). In other words, in the limit $z_0 \to 0$, the red curve of fig. 6(b) continuously falls on the ellipse given by eq. (23). In the experiments presented above, the radii and pitches of the helices of different chirality are closer to one another than in

the previous sections (for instance in fig. 2). It is a consequence of the negligible intrinsic torsion $\tau_0 \ll \kappa_0$ and of the small asymmetry of the helix compared to the circle.

Furthermore, expression of the axial force and torque by use of eq. (8), together with the fact that helices lie on the ellipse (23) yield that the set of connected helices in the case of zero intrinsic torsion correspond to coexisting helices with exactly zero axial torque. Using 8(a), we substitute τ in eq. (23) to obtain an equation linking the axial force in the rod and the curvature of the helices

$$\Gamma^2 T^2 / B^2 = [\kappa_0 - \kappa(1-\Gamma)]^3 (\kappa_0 - \kappa) \tag{24}$$

The corresponding curves are plotted as dashed lines in fig.13(b) and(c) for $\Gamma = 2/3$ and show good agreement with experimental data. Following McMillen and Goriely (2002) and Dilly et al. (2023), we take the straight rod limit $\kappa \to 0$ in eq. (24) and find that the axial force is finite and reads $T_c = B\kappa_0^2/\Gamma$, which corresponds to the writhing critical load. For axial forces close to this writhing critical force, we linearize eq. (24) and eq. (23) at leading order in $T_c - T$ and obtain

$$\kappa = \frac{2\Gamma(T_c - T)}{B\kappa_0(4-3\Gamma)} \tag{25a}$$

$$\tau = \pm\sqrt{\frac{2(T_c - T)}{B(4-3\Gamma)}} \tag{25b}$$

confirming both (*i*) the linear behavior of the increase of curvature at the onset of writhing instability observed in fig. 13(b), and (*ii*) the pitchfork bifurcation of the torsion as a function of the axial force evidenced in experiments of fig. 13(c), notably the slope one half in the log-log plot in fig. 13(e).

Finally, the expected curve for the writhing critical force, eq. (22), is plotted as a dashed line in fig. 13(d), with $B = E\pi d^4/64 = 2.6\times10^{-6}$ Pa·m^4 determined using the measured value of the Young Modulus $Y = 5$ MPa and $d = 1.8$ mm. This curve shows a good agreement with the experimental data.

The model of inextensible Kirchhoff rods and coexisting helices at equilibrium therefore allows us to quantitatively predict the behavior of an unwound helix at the writhing instability. The predicted writhing critical force agrees with experimental data, as well as the curvature and torsion behaviors and values upon this instability.

5. Discussion

There is an obvious analogy between the simple system presented here and liquid-gas phase transitions. Interestingly, the helical rods present a similar phase diagram as prestressed strips as recently reported by Gomez et al. (2023). The phase coexistence and accompanied plateau in $M(n)$ motivated us to construct the biphasic model (see section 3.2), which reproduces the phase diagram and overall $M(n)$ and $T(n)$ tendencies. The coexistence of the two phases occurs at almost constant torque, akin to the Maxwell plateau in phase transition. In a recent publication (Dilly et al., 2023) we showed that the equilibrium equations for the coexisting state can also be obtained through the minimization of the energy of the biphasic system, yielding equality of axial torque M and force T in the two helices. The minimization over the proportion α of phases (+) or (−) surprisingly led to the conservation of the I_1 integral defined in (9). In the phase transition analogy, the latter corresponds to equating the chemical potential of the two phases. Moreover, as stressed in section 3.2, trajectories in the (n, z) space can be found where the axial torque and force imposed to the mixed state (+/−) are rigorously constant, the only varying quantity being the proportion of phases (+) or (−), analog to the pressure-temperature diagram in liquid-gas transition.

To push further the analogy with the phase transitions, coexisting helices in mixed phase can be regarded as phases at equilibrium connected by an interface, the perversion, participating in the total energy of the system. The injection of the perversion from one end and the energy barrier of this injection leads to a jump in the torque and force curves $M(n)$ and $T(n)$ (see fig. 2) related to the metastability of the $(+/-)$ state, analogous to a nucleation phenomenon. The perversion would be analogous to the phase boundary between gas and liquid, invoking the surface tension and corresponding nucleation barrier for bubble nucleation. The biphasic model ignores the effects of perversion and boundaries (clamps), and for this reason misses the nucleation, that is the snapping from helix to perversion. In order to include these nucleation effects, we solve the problem using numerical simulations with the library AUTO. The resulting profile $M(n)$ closely reproduces the experimental data. In order to decipher the singular first-order-like transitions between single helix and mixed state we focus on all possible stationary branches as shown in fig. 11(b). In between coexisting stable branches there are unstable ones, indicating the sub-critical nature of the transitions. The jumps occur when two stable branches coexist, as is the case near the limits of the mixed phase. In an unwinding experiment, one starts on the $(+)$ branch and follows it as long as it exists. When it disappears (near $n/n_0 \approx 0.5$ in the depicted case), the system abruptly jumps onto the mixed $(+/-)$ phase. As we proceed with unwinding, the system follows the same logic, remaining on the actual stable branch as long as the branch exists. For obvious reasons, visible in the figure, the mixed $(+/-)$ phase disappears toward the $(-)$ branch with a much weaker jump. This asymmetry between injection and expulsion events is clearly visible in experiments.

A question one could ask is whether it is possible to find a way to quasi-statically inject the perversion continuously, without snapping. The answer is yes, there exists at least one way to do it, and it is to simulate by the clamp the arrival of a perversion from behind, as if there was no clamp. There are other ways of doing it, as we observed when preparing a perversion conformation for ABAQUS simulations (see sec. 3.3.2 and Supplemental Material (Dilly et al., 2024, videos 4 and 5)). The important point here is that the amplitude and the strength of the singularity at perversion creation are operator dependent and that this singularity can be even completely eliminated. This bring to mind the phenomena of inducing nucleation of bubbles by controlled surfaces, impurities, or local mechanical shocks that help germination.

Another singular event: the jump of the perversion to a self contact is discussed in sec. 3.3.2 (blue line in fig. 5). The transition is easily comprehended qualitatively by simple observation of the experiment shown in fig. 10. The most intriguing about this transition is how it can be detected by theoretical means. We used shooting method and ABAQUS to find equilibrium configurations of the system as described by continuous and differentiable set of variables: for instance three curvatures and three forces. But the self-contact solution lies out of the reach of this strategy because at self-contact there is a singularity in configuration variables. Moreover, the internal constraint at the contact depends on the friction and geometry of the rod cross-section. Nevertheless, we are able to find the jump simply by finding the critical value T_p of the force T at which the stable solution ceases to exist. We use the same reasoning as in the case of perversion injection (see sec. 3.4 and fig. 11): we identify the endpoint of a stable branch as a limit point where snapping occurs. The difference here is that we do not know where the system jumps and if there is a unique stable branch to jump on. Probably it is not unique because of nonholonomic (dynamics-dependent) property of the contact constraint. It is likely that there exists a continuum of self-contact configurations parameterized by the static friction in the contact. Shooting and ABAQUS methods give the same critical condition for destabilization of perversion. Strictly mathematically speaking the above does not determine what happens on the other side of the transition, i.e. when $T < T_p$, but in this very point we trust the experiment: all these configurations have a self-contact.

The culminating point of the phase diagram in fig. 5, corresponds to the point $z/L = 1$, and $n = 0$. At this point, the system is achiral. The rod is straight, with no twist, therefore, corresponding to a point at which chirality is not defined. The system is neither in the $(+)$ or $(-)$ phase. This is the case of plant tendrils attached to a support: at the beginning of its development the straight tendril attaches to support and then starts to coil, creating two opposite helices with a perversion. In this regard our detailed study of $n = 0$ case has a bioinspired dimension. A detailed study of living plant tendril growth and mechanics in terms of both Kirchhoff model of rods and a plant growth model

is discussed by Dilly (2024). Our experiments confirm that the transition from straight to writhed conformation is supercritical, as the curvature scales as ~~like~~ **Emilien:** $T_c - T$. Another accessible example of the writhing instability can be observed in everyday life by combing curly hair. The action of combing removes the winding n in the hair, while extending it. The hair is then in the straight and twistless configuration, i.e. $z = L$ and $n = 0$. Once the hair comb is removed, the extension z of the hair shortens, and the writhing instability kicks in, but dynamically, conversely to our quasi-static experiments. Inertia effects maintain the $n = 0$ constraint enabling the creation of the perversion. Finally, friction induced by self-contact freezes the perverted configurations. This effect has been discussed and reproduced numerically by Crespel et al. (2024). In addition to perversion nucleation/annihilation and jump to self contact, the writhing transition concludes the zoology of critical phenomena of helical rods upon quasi-static unwinding with perversion.

Finally, the system also makes it possible to create two perversions within the rod or multiple perversion conformations, as illustrated and studied by Domokos and Healey (2005). From the point of view of the biphasic model, any number of perversions is allowed, since only pure phases enter into calculation. We know that this is not sufficient because (i) perversions have their energy and (ii) perversion can interact. For above reasons the system itself prefers to nucleate only one perversion at its endpoint: we have an example of heterogeneous nucleation, i.e. the "bubble" prefers to nucleate at the boundary. However, configurations with any number of perversions are stable once they are generated. These issues are discussed by Dilly (2024).

6. Conclusion

Critical phenomena invoking perversion in helical elastic rods were studied as function of extension z and number of turns n. All transitions are presented in the phase diagram of fig. 5. 1) The red curve is the transition between pure, (+) or (-), helical states and the mixed (+/-) state, in which two opposite helices are connected by a perversion. The transition is subcritical as the intensive variables M and T have finite jumps at the transition. The jumps correspond to snapping at injection/annihilation of perversion. As the winding varies within the mixed state, M remains almost constant. Jumps at transition and the Maxwell-like plateau are well-known signatures of the first-order phase transitions, for instance the liquid-gas transition. The nucleation of perversion is therefore analogous to the creation of critical bubbles giving rise to phase-separated states. 2) The blue line in fig. 10(a) marks the instability of the perversion toward self-contact. Is is another subcritical jump, delimiting the regime where the perversion can smoothly travel (above the line) and the regime where configurations are determined by self-contact and their corresponding to nonholonomic constraints. Theoretically, the transition can be seen as a breakdown of heteroclinic path between two opposite helices. 3) The writhing transition, shown in fig. 10(a), is supercritical. Near critical force T_c, it is characterized by a typical square-root scaling of the twist curvature τ as function of $T_c - T$. The understanding of the writhing transition at zero winding is the basis of quantitative understanding of force generation by plant tendrils, as discussed by Dilly (2024).

Snapping transitions, associated with subcritical behavior in elastic rods are relevant for the interpretation of singular events in any axially forced helix. Application to soft and nano-robotics can be envisaged, wherever rapid actuated mechanical action is needed. In the context of plant tendril development and possible bionic and hybrid systems, our findings could allow one to control the way in which slowly developing plants can produce rapid snaps.

Supplemental material

Supplemental material including videos, codes and data are available on-line (Dilly et al., 2024).

Acknowledgement

The present research is a part of DynaVine action supported by the IdEX Université Paris Cité, ANR-18- IDEX-0001.

Appendix A. The limit of the domain of coexistence

We focus on the $n/n_0 \geq 0$ part of the curve setting the limit of the coexistence region in the (n, z) plane. The curve was drawn red in figure 5 for the case $z_0/L = 0.2$ and we study here how it changes when z_0/L is changed.

Appendix A.1. The $z/L \to 1$ limit

We first focus on the part of the curve near $z/L = 1$. Dilly et al. (2023) stated that, as $z/L \to 1$, the shape of this curve is parabolic, with the symmetry $n \to -n$

$$\frac{n}{n_0} \underset{z\to L}{=} \sqrt{1-Z^2}\, h(\Gamma, Z_0) \tag{A.1}$$

where $Z = z/L$ and $Z_0 = z_0/L$. Please note that when $z_0 = 0$ formula (A.1) matches the $z/L \to 1$ limit of formula (A.9). The force and torque are then given by

$$\frac{T\,R_0^2}{B} \underset{z\to L}{=} (1-Z_0^2)^{3/2}\, h(\Gamma, Z_0) \tag{A.2}$$

$$\frac{M\,R_0}{B} \underset{z\to L}{=} -\Gamma\, Z_0\, \sqrt{1-Z_0^2} \tag{A.3}$$

Please note that when $z_0 = 0$, we have $h(\Gamma, Z_0 = 0) = 1/\Gamma$ and formulas (A.2) and (A.3) coincide with the force and torque at the writhing transition, see eq. (22). On this curve, each point on the right side is connected to a point $(n_b/n_0, Z_b)$ of the left side (see for example the dotted brown lines in fig. 8) with

$$\frac{n_b}{n_0} \underset{z\to L}{=} -\frac{(1-Z_b)\Gamma Z_0 + \sqrt{1-Z_b^2}\,\sqrt{1-Z_0^2}}{1-(1-\Gamma)\,Z_b^2} \tag{A.4}$$

where Z_b is the real root of the 5^{th} degree polynomial

$$P(Z_b) = P_0 + (4\Gamma-3)P_1 Z_b + 2(\Gamma-1)(2\Gamma-1)P_0 Z_b^2 + 2(1-\Gamma)P_1 Z_b^3 - 3(1-\Gamma)^2 P_0 Z_b^4 + (1-\Gamma)^2 P_1 Z_b^5 \tag{A.5}$$

$$\text{with} \quad P_0 = -1 + \Gamma^2 + (1+\Gamma^2)(2Z_0^2 - 1) \tag{A.6}$$

$$P_1 = 1 + \Gamma^2 - (1-\Gamma^2)(2Z_0^2 - 1) \tag{A.7}$$

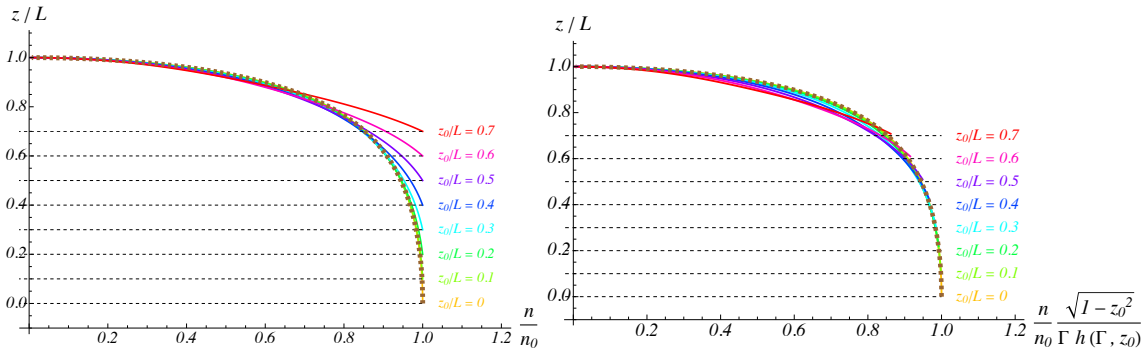

Figure A.15: The limit of the coexistence region for $n/n_0 \geq 0$ for different values of z_0/L. Colored curves are computed numerically as explained in section 3. (Left) We compare the analytical formula (A.9) to these numerical results and see it only works for small values of z_0/L. (Right) We show that the analytical formula (A.10) gives a good approximation of the limit of the coexistence region even for larger values of z_0/L. In both cases the thick dotted brown curve is parametrically defined by $\left\{\frac{\sqrt{1-Y^2}}{1-(1-\Gamma)Y^2}, Y\right\}$ with $Y \in (0;1)$. Fixed parameter: $\Gamma = 2/3$.

The parameter $h(\Gamma, Z_0)$ is given by

$$h(\Gamma, Z_0) = \Gamma \frac{\left[Z_b\sqrt{1-Z_0^2} + Z_0(1-(1-\Gamma)Z_b)\sqrt{1-Z_b^2}\right]\left[\sqrt{1-Z_b^2}\sqrt{1-Z_0^2} + \Gamma Z_0(1-Z_b)\right]}{\sqrt{1-Z_b^2}\sqrt{1-Z_0^2}\left(1-(1-\Gamma)Z_b^2\right)^2} \tag{A.8}$$

For $z_0/L = 0.2$ and $\Gamma = 2/3$, as $z/L \to 1$, we have $T \simeq 1.39$, $M \simeq -0.13$, $n_b/n_0 = -0.13$, $h \simeq 1.48$, and $Z_b = 0.996$. Please note that this approximation works correctly even as z/L moves away from 1, as long as z remains significantly larger than z_0.

Appendix A.2. An approximate formula for the limit of coexistence for all z_0/L values

We now consider the entire (positive part) of the the limit of the coexistence region in the (n, z) plane. In the case $z_0 = 0$, McMillen and Goriely (2002) showed that this limit of the domain of coexistence is given by

$$\left.\frac{n}{n_0}\right|_{z_0=0} = \frac{\sqrt{1-(z/L)^2}}{1-(1-\Gamma)(z/L)^2} \tag{A.9}$$

In the case $z_0 > 0$ we have no such closed-form solution to offer to the reader, but the approximate formula

$$\frac{n}{n_0} \approx \frac{\sqrt{1-(z/L)^2}}{1-(1-\Gamma)(z/L)^2} \frac{\Gamma\, h(\Gamma, z_0/L)}{\sqrt{1-(z_0/L)^2}} \tag{A.10}$$

seems to work nicely over a wide range of z_0 values, see fig. A.15.

Appendix B. Stereoscopy and rod 3D reconstruction

Two Nikon® 3300 cameras were placed around the experimental setup approximately at a 90 degree angle in the horizontal plane. Pose estimation of the cameras and camera calibration were performed using printed checker boards

together with built-in functions of the python library OpenCV. The followed method can be found in OpenCV (2024). The intrinsic matrix of the cameras was obtained on a series of approximately a hundred photos of a checkerboard with the function cv.calibrateCamera. From a set of photos of a checker board visible by both cameras, the rotation matrix, the translation vector and the fundamental matrix of the apparatus were then computed with a built-in function of OpenCV: cv.stereoCalibrate.

The writhing experiment was conducted within the field of view of two cameras. In each photo, the edges of the rod were identified, and the centerline of the rod was calculated by determining the midpoint between the two edges along the normal direction to a given edge. Using this method, the centerline of the rod was extracted from both photos, yielding the 2D coordinates of the centerline in the plane of each camera. The correspondence problem was solved using epilines computed via the built-in OpenCV function cv.computeCorrespondEpilines. Since the centerline is one-dimensional and the cameras are fixed such that the epilines intersect the 2D curve in the other camera's image at a unique point, this approach ensured reliable matching. With the calibration parameters, the fundamental matrix of the apparatus, and the 2D views of the centerline, the centerline's 3D coordinates were reconstructed in the laboratory frame using the OpenCV function cv.triangulatePoints. The 3D reconstructed rod along the writhing experiment is shown in Supplemental Material (Dilly et al., 2024, video 3). The tangent vector along the rod was then computed using a finite difference method at every point along the centerline. To reduce numerical noise, smoothing was applied over an arc-length window that was small relative to the typical scale of variation in the tangent vector components. The straight rod at the start of the writhing experiment was used to establish the reference frame, ensuring that the tangent vector in this configuration was defined as $\mathbf{t} = (0, 0, 1)$. After the onset of the writhing instability, in the helical segments of the rod, a helical pattern of the type

$$\mathbf{t} = (\sin(\theta)\cos(\lambda s), \sin(\theta)\sin(\lambda s), \cos\theta) \tag{B.1}$$

was fitted on θ and λ to the tangent vector components. This estimation of θ and λ gives the curvature and torsion in the helical patterns with the relations $\kappa = \lambda\sin(\theta)$ and $\tau = \lambda\cos(\theta)$.

References

Aldinger, J., Klapper, I., Tabor, M., 1995. Formulae for the calculation and estimation of writhe. Journal of Knot Theory and its Ramifications 4, 343–372. doi:10.1142/S021821659500017X.

Allemand, J.F., Bensimon, D., Lavery, R., Croquette, V., 1998. Stretched and overwound DNA forms a Pauling-like structure with exposed bases. Proceedings of the National Academy of Sciences of the USA 95, 14152–14157. doi:10.1073/pnas.95.24.14152.

Antman, S.S., 2004. Nonlinear problems of elasticity. 2nd ed., Springer-Verlag, New York.

Armanini, C., Boyer, F., Mathew, A.T., Duriez, C., Renda, F., 2023. Soft robots modeling: A structured overview. IEEE Transactions on Robotics 39, 1728–1748. doi:10.1109/TRO.2022.3231360.

Audoly, B., Pomeau, Y., 2010. Elasticity and Geometry: From Hair Curls to the Non-linear Response of Shells. Oxford University Press.

Berger, M.A., Prior, C., 2006. The writhe of open and closed curves. Journal of Physics A: Mathematical and General 39, 8321–8348. doi:10.1088/0305-4470/39/26/005.

Borum, A., Bretl, T., 2020. Infinitely long isotropic kirchhoff rods with helical centerlines cannot be stable. Physical Review E 102, 023004. doi:10.1103/PhysRevE.102.023004.

Bryant, Z., Stone, M.D., Gore, J., Smith, S.B., Cozzarelli, N.R., Bustamante, C., 2003. Structural transitions and elasticity from torque measurements on DNA. Nature 424, 338–341. doi:10.1038/nature01810.

Bustamante, C., Yan, S., 2022. The development of single molecule force spectroscopy: From polymer biophysics to molecular machines. Quarterly Reviews of Biophysics 55, 1–49.

Canejo, J.P., Godinho, M.H., 2013. Cellulose Perversions. Materials 6, 1377–1390. doi:10.3390/ma6041377.

Champneys, A.R., Thompson, J.M.T., 1996. A multiplicity of localized buckling modes for twisted rod equations. Proceedings of the Royal Society of London. Series A: Mathematical, Physical and Engineering Sciences 452, 2467–2491. doi:10.1098/rspa.1996.0135.

Chouaieb, N., Goriely, A., Maddocks, J.H., 2006. Helices. Proceedings of the National Academy of Sciences 103, 9398–9403. doi:10.1073/pnas.0508370103.

Cook, T.A., 1979. The Curves of Life. Reprint edition ed., Dover Publications, New York. Originally published in 1914 by Constable and Company, London.

Crespel, O., Hohnadel, E., Métivet, T., Bertails-Descoubes, F., 2024. Contact detection between curved fibres: high order makes a difference. ACM Transactions on Graphics 43, 132:1–23. doi:10.1145/3658191.

Călugăreanu, G., 1959. L'intégrale de Gauss et l'analyse des noeuds tridimensionnels. Rev. Math. Pures Appl. 4, 5–20.
Dai, L., Zhu, K.D., Shen, W., Huang, X., Zhang, L., Goriely, A., 2018. Controllable rotational inversion in nanostructures with dual chirality. Nanoscale 10, 6343–6348. doi:10.1039/C7NR09035H.
Darwin, C., 1865. On the movements and habits of climbing plants. Cambridge University Press.
Dilly, E., 2024. Helices, Perversions and Tendrils: from Plant-Inspired Rod Mechanics to Curvature Generation in Tendril Bearing Plants. Ph.D. thesis. Université Paris Cité. URL: https://theses.fr/s301379. PhD thesis under the direction of Dražen Zanchi and Julien Derr, Physics department, Université Paris Cité.
Dilly, E., Neukirch, S., Derr, J., Zanchi, D., 2023. Traveling Perversion as Constant Torque Actuator. Phys. Rev. Lett. 131, 177201. doi:10.1103/PhysRevLett.131.177201.
Dilly, E., Neukirch, S., Derr, J., Zanchi, D., 2024. Supplemental material for: Critical phenomena in helical rods with perversion. doi:10.6084/m9.figshare.28014872.
Doedel, E., Keller, H.B., Kernevez, J.P., 1991. Numerical Analysis And Control of Bifurcation Problems (II): Bifurcation In Infinite Dimensions. International Journal of Bifurcation and Chaos 1, 745–772. doi:10.1142/S0218127491000555.
Domokos, G., Healey, T.J., 2005. Multiple Helical Perversions of Finite, Intrinsically Curved Rods. International Journal of Bifurcation and Chaos 15, 871–890. doi:10.1142/S0218127405012430.
Forterre, Y., Dumais, J., 2011. Generating Helices in Nature. Science 333, 1715–1716. doi:10.1126/science.1210734.
Fuller, F.B., 1971. The writhing number of a space curve. Proceedings of the National Academy of Sciences of the USA 68, 815–819. doi:10.1073/pnas.68.4.815.
Fuller, F.B., 1978. Decomposition of the linking number of a closed ribbon: A problem from molecular biology. Proceedings of the National Academy of Sciences of the USA 75, 3557–3561. doi:10.1073/pnas.75.8.3557.
Gerbode, S.J., Puzey, J.R., McCormick, A.G., Mahadevan, L., 2012. How the Cucumber Tendril Coils and Overwinds. Science 337, 1087–1091. doi:10.1126/science.1223304.
Goldstein, R.E., Goriely, A., Huber, G., Wolgemuth, C.W., 2000. Bistable Helices. Phys. Rev. Lett. 84, 1631–1634. doi:10.1103/PhysRevLett.84.1631.
Gomez, M., Reis, P.M., Audoly, B., 2023. Twisting instabilities in elastic ribbons with inhomogeneous pre-stress: A macroscopic analog of thermodynamic phase transition. Journal of the Mechanics and Physics of Solids 181, 105420. doi:10.1016/j.jmps.2023.105420.
Goriely, A., Tabor, M., 1998. Spontaneous helix hand reversal and tendril perversion in climbing plants. Physical Review Letters 80, 1564–1567. doi:10.1103/PhysRevLett.80.1564.
Goriely, A., Tabor, M., 2013. Rotation, inversion and perversion in anisotropic elastic cylindrical tubes and membranes. Proceedings of the Royal Society A: Mathematical, Physical and Engineering Sciences 469, 20130011. doi:10.1098/rspa.2013.0011.
Jones, T.J., Jambon-Puillet, E., Marthelot, J., Brun, P.T., 2021. Bubble casting soft robotics. Nature 599, 229–233. doi:10.1038/s41586-021-04029-6.
Kirchhoff, G., 1859. Über das Gleichgewicht und die Bewegung eines unendlich dünnen elastischen Stabes. J. Reine Angew. Math. 56, 285–313.
Listing, J.B., 1848. Vorstudien zur Topologie. Vandenhoeck und Ruprecht, Gottingen.
Liu, J., Huang, J., Su, T., Bertoldi, K., Clarke, D.R., 2014. Structural Transition from Helices to Hemihelices. PLOS ONE 9, 1–7. doi:10.1371/journal.pone.0093183.
Liu, S., Yao, Z., Chiou, K., Stupp, S.I., Olvera de la Cruz, M., 2016. Emergent perversions in the buckling of heterogeneous elastic strips. Proceedings of the National Academy of Sciences 113, 7100–7105. doi:10.1073/pnas.1605621113.
Love, A.E.H., 1990. A treatise on the mathematical theory of elasticity. 4th ed., Dover.
Lutz-Bueno, V., Bolisetty, S., Azzari, P., Handschin, S., Mezzenga, R., 2020. Self-Winding Gelatin–Amyloid Wires for Soft Actuators and Sensors. Advanced Materials 32, 2004941. doi:10.1002/adma.202004941.
Marko, J.F., Neukirch, S., 2013. Global force-torque phase diagram for the DNA double helix: Structural transitions, triple points, and collapsed plectonemes. Phys. Rev. E 88, 062722. doi:10.1103/PhysRevE.88.062722.
Maxwell, J., 1873. A Treatise on Electricity and Magnetism. Clarendon Press, Oxford.
McGuffee, A.E., Doughty, E.R., Grewal, G.S., Dinner, A.R., 2023. Bend or twist? what plectonemes can teach us about helical bacteria. Physical Review Letters 131, 178401. URL: https://doi.org/10.1103/PhysRevLett.131.178401.
McMillen, Goriely, 2002. Tendril Perversion in Intrinsically Curved Rods. Journal of Nonlinear Science 12, 241–281. doi:10.1007/s00332-002-0493-1.
Mehling, J., Diftler, M., Chu, M., Valvo, M., 2006. A Minimally Invasive Tendril Robot for In-Space Inspection, in: The First International Conference on Biomedical Robotics and Biomechatronics, IEEE. pp. 690–695. doi:10.1109/BIOROB.2006.1639170.
Nakane, D., Ito, T., Nishizaka, T., 2020. Coexistence of Two Chiral Helices Produces Kink Translation in *Spiroplasma* Swimming. Journal of Bacteriology 202, e00735–19. doi:10.1128/JB.00735-19.
OpenCV, 2024. OpenCV-Python: Camera Calibration and 3D Reconstruction. URL: https://docs.opencv.org/4.x/d6/d00/tutorial_py_root.html.
Prior, C.B., Neukirch, S., 2016. The extended polar writhe: a tool for open curves mechanics. Journal of Physics A: Mathematical and Theoretical 49, 215201. doi:10.1088/1751-8113/49/21/215201.
Riccobelli, D., Noselli, G., DeSimone, A., 2021. Rods coiling about a rigid constraint: helices and perversions. Proceedings of the Royal Society A: Mathematical, Physical and Engineering Sciences 477, 20200817. doi:10.1098/rspa.2020.0817.
Sarkar, A., Léger, J.F., Chatenay, D., Marko, J.F., 2001. Structural transitions in DNA driven by external force and torque. Physical Review E 63, 051903. doi:10.1103/PhysRevE.63.051903.
Silva, P.E.S., Trigueiros, J.L., Trindade, A.C., Simoes, R., Dias, R.G., Godinho, M.H., de Abreu, F.V., 2016. Perversions with a twist. Scientific Reports 6, 23413. URL: http://www.nature.com/articles/srep23413, doi:10.1038/srep23413.
Strick, T.R., Allemand, J.F., Bensimon, D., Bensimon, A., Croquette, V., 1996. The elasticity of a single supercoiled DNA molecule. Science 271, 1835–1837. doi:10.1126/science.271.5257.1835.
Strogatz, S.H., 1994. Nonlinear Dynamics and Chaos. Perseus Books.

Timoshenko, S.P., Gere, J.M., 1961. Theory of Elastic Stability. 2nd ed., McGraw-Hill.
Wang, D., Thouless, M., Lu, W., Barber, J., 2020. Generation of perversions in fibers with intrinsic curvature. Journal of the Mechanics and Physics of Solids 139, 103932. doi:https://doi.org/10.1016/j.jmps.2020.103932.
Zhou, Z., Joós, B., Lai, P.Y., Young, Y.S., Jan, J.H., 2007. Elasticity and stability of a helical filament with spontaneous curvatures and isotropic bending rigidity. Modern Physics Letters B 21, 1895–1913. doi:10.1142/S0217984907014058.